Cell Reports
Medicine

Article

Combinatorial targeting of glutamine metabolism and lysosomal-based lipid metabolism effectively suppresses glioblastoma

Graphical abstract

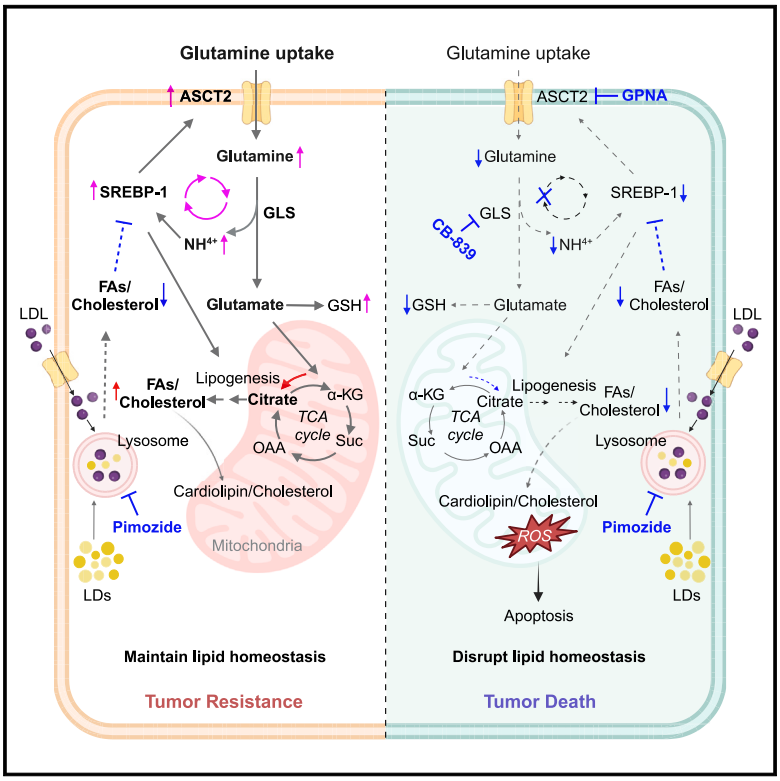

Highlights

- Pimozide inhibits lysosome function while stimulating glutamine consumption in GBM
- Pimozide activates SREBP-1 that promotes glutamine uptake by upregulating ASCT2
- Combining lysosome and glutamine inhibition severely impairs mitochondria in GBM
- This combination significantly suppresses GBM growth *in vitro* and *in vivo*

Authors

Yaogang Zhong, Feng Geng, Logan Mazik, ..., Xiang Zhang, Arnab Chakravarti, Deliang Guo

Correspondence

deliang.guo@osumc.edu

In brief

Zhong et al. report that GBM resists the antipsychotic drug pimozide treatment by activating SREBP-1, which unexpectedly elevates glutamine consumption by upregulating the expression of ASCT2. They demonstrate combining pimozide with a pharmacological blockade of glutamine consumption effectively inhibits GBM growth *in vivo*, presenting a promising avenue for targeting GBM.

Zhong et al., 2024, Cell Reports Medicine *5*, 101706
September 17, 2024 © 2024 The Author(s). Published by Elsevier Inc.
https://doi.org/10.1016/j.xcrm.2024.101706

CellPress

Cell Reports Medicine

CellPress
OPEN ACCESS

Article

Combinatorial targeting of glutamine metabolism and lysosomal-based lipid metabolism effectively suppresses glioblastoma

Yaogang Zhong,[1,2] Feng Geng,[1,2] Logan Mazik,[1,2] Xinmin Yin,[3] Aline Paixao Becker,[1] Shabber Mohammed,[4] Huali Su,[1,2] Enming Xing,[4] Yongjun Kou,[1,2] Cheng-Yao Chiang,[1,2] Yunzhou Fan,[1,2] Yongchen Guo,[1,2] Qiang Wang,[1,2] Pui-Kai Li,[4] Xiaokui Mo,[5] Etienne Lefai,[6] Liqing He,[3] Xiaolin Cheng,[4,7] Xiang Zhang,[3] Arnab Chakravarti,[1] and Deliang Guo[1,2,8,*]

[1]Department of Radiation Oncology, Ohio State Comprehensive Cancer Center, Arthur G. James Cancer Hospital and Richard J. Solove Research Institute, and College of Medicine at The Ohio State University, Columbus, OH 43210, USA

[2]Center for Cancer Metabolism, The Ohio State University Comprehensive Cancer Center, Columbus, OH 43210, USA

[3]Department of Chemistry, Center for Regulatory and Environmental Analytical Metabolomics, University of Louisville, Louisville, KY 40208, USA

[4]Division of Medicinal Chemistry & Pharmacognosy, College of Pharmacy at The Ohio State University, Columbus, OH 43210, USA

[5]Center for Biostatistics, Department of Biomedical Informatics, College of Medicine, The Ohio State University, Columbus, OH 43210, USA

[6]Human Nutrition Unit, French National Research Institute for Agriculture, Food and Environment, University Clermont Auvergne, 63122 Clermont-Ferrand, France

[7]Translational Data Analytics Institute at The Ohio State University, Columbus, OH 43210, USA

[8]Lead contact

*Correspondence: deliang.guo@osumc.edu

https://doi.org/10.1016/j.xcrm.2024.101706

SUMMARY

Antipsychotic drugs have been shown to have antitumor effects but have had limited potency in the clinic. Here, we unveil that pimozide inhibits lysosome hydrolytic function to suppress fatty acid and cholesterol release in glioblastoma (GBM), the most lethal brain tumor. Unexpectedly, GBM develops resistance to pimozide by boosting glutamine consumption and lipogenesis. These elevations are driven by SREBP-1, which we find upregulates the expression of ASCT2, a key glutamine transporter. Glutamine, in turn, intensifies SREBP-1 activation through the release of ammonia, creating a feedforward loop that amplifies both glutamine metabolism and lipid synthesis, leading to drug resistance. Disrupting this loop via pharmacological targeting of ASCT2 or glutaminase, in combination with pimozide, induces remarkable mitochondrial damage and oxidative stress, leading to GBM cell death *in vitro* and *in vivo*. Our findings underscore the promising therapeutic potential of effectively targeting GBM by combining glutamine metabolism inhibition with lysosome suppression.

INTRODUCTION

Over the past two decades, there has been no significant progress in the therapy for glioblastoma (GBM), which has a median survival of only 12–16 months from diagnosis despite extensive treatments.[1,2] GBM is a very aggressive cancer, and at diagnosis its tumor cells have already invaded into the surrounding normal brain tissue, rendering complete surgical resection, an ineffective therapeutic option.[2] Additionally, the presence of the blood-brain barrier (BBB) restricts the penetration of many potent antitumor drugs into GBM tissues, making GBM one of the most difficult cancers to treat.[3]

Recent investigations have revealed the potential of certain brain-penetrant antipsychotic drugs to induce cell death in GBM cells *in vitro*.[4,5] However, these promising effects are difficult to reproduce *in vivo* in intracranial GBM models.[6] The inconsistency between *in vitro* and *in vivo* studies may be attributed to two factors: first, the *in vivo* administration of these drugs could not achieve an effective dose capable of efficiently eliminating tumor cells, due to a toxicity concern in normal tissues; and second, tumor cells could rapidly develop resistance to intracranially delivered drugs.[7–9] Our primary objective was 2-fold: to identify a potent brain-penetrant drug capable of effectively treating GBM at a safe dose in a preclinical model, while concurrently developing a strategy to prevent the development of tumor resistance.

In this study, we discovered that the antipsychotic drug pimozide exhibits inhibitory effects on GBM cell viability. However, GBM cells acquire resistance to this therapy by upregulating glutamine metabolism. By targeting glutamine uptake or consumption, we uncovered a potent synergy with pimozide, overcoming tumor resistance and effectively eradicating GBM cells both *in vitro* and *in vivo* settings. This combination treatment holds promise for translation into clinical trials, not only as a potential therapy for GBM but also for other aggressive tumor types reliant on glutamine and lipids for sustenance.

This is an open access article under the CC BY-NC-ND license (http://creativecommons.org/licenses/by-nc-nd/4.0/).

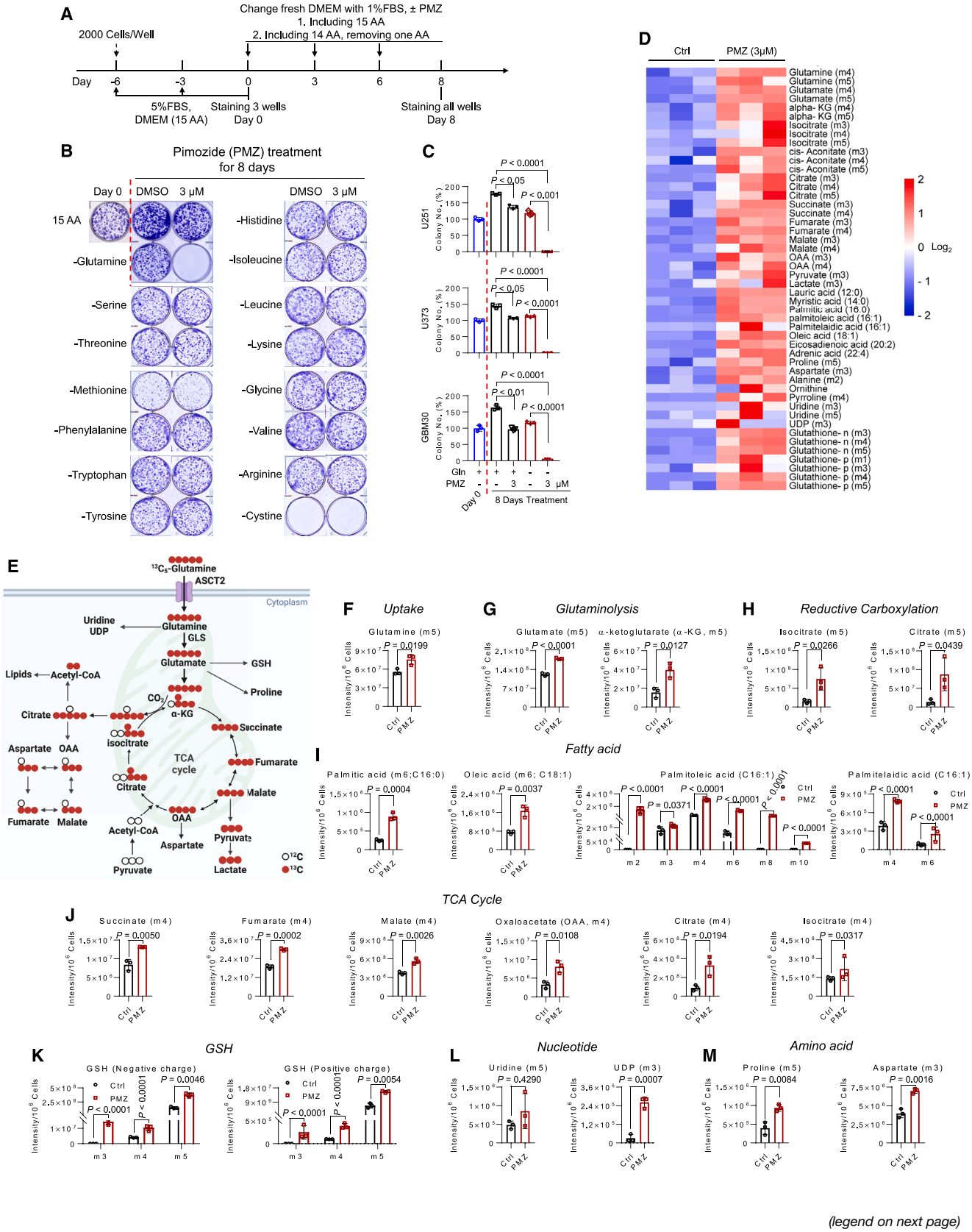

(legend on next page)

CellPress
OPEN ACCESS

RESULTS

Limiting glutamine availability sensitizes GBM to pimozide-based treatment

We examined the cytotoxic effects of nine Food and Drug Administration-approved antipsychotic drugs previously reported for their potential antitumor activities[10–13] in GBM cell lines U251 and U373 and patient-derived primary GBM30 cells. Our investigation revealed that pimozide, a medication used for the treatment of schizophrenia,[14,15] as well as motor and phonic tics associated with Tourette's syndrome,[16,17] exhibited the highest potency *in vitro* against all these GBM cells (Figure S1A). Notably, the antitumor properties of pimozide were recognized as far back as the 1970s, demonstrated in pituitary tumor cell lines and rat models.[18] Subsequent research on this drug has persisted, exploring its potential for various types of cancers in preclinical models.[19–21] Additionally, in the 1980s, a phase 2 clinical trial involving 30 patients with metastatic melanoma investigated pimozide's effectiveness, yielding partial responses in six of the patients.[22] Since this trial, no further cancer trials with pimozide have been reported.

Recent studies have underscored the critical roles of specific amino acids, notably, glutamine, methionine, lysine, and arginine, in fueling tumor growth.[23–27] We set out to investigate whether limiting amino acid availability could enhance the sensitivity of GBM to pimozide treatment. We cultured three different GBM cells for 6 days in a full DMEM medium that contains 15 amino acids until colonies formed (Figures 1A, 1B, and S1B). Subsequently, we replaced the complete medium with a fresh medium, each lacking one of the 15 amino acids, followed by treatment with/without pimozide in the presence of 1% fetal bovine serum (FBS). Unexpectedly, limiting glutamine availability led to a profound effect: pimozide at 3 μM nearly completely eradicated pre-existing colonies and effectively killed GBM cells (Figures 1B, 1C, and S1B–S1D). In contrast, when used at the same dose in the complete medium, pimozide only exhibited mild inhibition of colony growth (Figures 1B, 1C, and S1B–S1D). Intriguingly, removal of any other amino acids failed to heighten pimozide sensitivity (Figures 1B, 1C, and S1B). Notably, cystine (Cys), crucial in regulating cellular redox homeostasis,[28,29] was found to be vital for GBM colony maintenance (Figures 1B and S1B), emphasizing the critical role of redox balance in GBM viability.

Pimozide enhances glutamine consumption and promotes reductive carboxylation-mediated lipid synthesis

We proceeded to investigate the role of glutamine in pimozide sensitivity. We conducted a stable isotope $^{13}C_5$-glutamine flux assay coupled with untargeted metabolomics analysis using liquid chromatography-tandem mass spectrometry (LC-MS/MS) in GBM cells. Notably, pimozide treatment exhibited a remarkable increase in virtually all facets of glutamine metabolism (Figures 1D–1M and S2A–S2D). These encompassed elevated glutamine uptake (Figure 1F), intensified glutaminolysis (Figures 1G and S2A), heightened reductive carboxylation (Figure 1H) and the subsequent *de novo* fatty acid (FA) synthesis it drives (Figures 1I and S2B), augmented tricarboxylic acid (TCA) cycle anaplerosis (Figures 1J and S2C), and intensified synthesis of glutathione (GSH) (Figure 1K), nucleotides (Figure 1L), and other amino acids, namely proline and aspartate (Figures 1M and S2D). These findings strongly suggest that the upregulation of glutamine uptake and consumption potentially serves as a survival mechanism for GBM cells under pimozide treatment.

Pimozide diminishes membrane cholesterol levels by inhibiting lysosome-mediated lipid droplet and lipoprotein hydrolysis

To investigate how pimozide induces the upregulation of glutamine metabolism, we employed Pacific blue, a fluorescent molecule, to label the drug (Figures 2A, S3A, and S3B). This enabled us to examine its subcellular distribution within GBM cells. Fluorescence imaging revealed that Pacific blue-labeled pimozide predominantly accumulated within the lysosomes, as confirmed by co-staining with LysoTracker (Figure 2B). We did not observe Pacific blue-labeled pimozide localization in the plasma membrane, as indicated by CellMask staining (green) (Figure 2B), mitochondria (MitoTracker, green) (Figure S3C), or endoplasmic reticulum (ER) (mCherry-labeled ER protein marker Sec61) (Figure S3D). In contrast, Pacific blue specifically attached to the plasma membrane through the linker (octanamine) (Figure 2B), while Pacific blue alone, without the linker, did not bind to the cells (Figure S3E).

Pimozide is characterized by its amphiphilic nature and includes an amine group with a pKa of approximately 8.6 (Figure 2A). We next tested whether pimozide penetrates lysosomes, which typically maintain a pH 4.5–5.0, and affects their pH. By using LysoSensor Yellow/Blue dextran, a pH-sensitive

Figure 1. Pimozide upregulates glutamine metabolism in GBM cells

(A) Schematic diagram illustrating the development of GBM colonies for drug treatment.

(B and C) Effects of pimozide treatment for 8 days on established U251 cells-derived colonies ($n = 3$ independent experiments) in DMEM medium containing 1% FBS in the presence and absence of the indicated amino acids (AA) (B) Day 0 indicates the pre-formed colonies before treatment. Colony numbers were quantified by ImageJ and normalized with the number of control cells in a full DMEM medium without drug treatment (mean ± SD, $n = 3$) (C). Statistical significance was determined by one-way ANOVA with Dunnett's multiple comparisons adjustments.

(D and E) Heatmap of metabolomics analysis of U251 cells supplemented with ^{13}C5-glutamine (2 mM) for 1 h after treatment with pimozide (PMZ, 3 μM) for 24 h (D). The results are from three biological replicates and summarized by the indicated schematic diagram (E). ^{13}C carbons are shown as red circles, and ^{12}C carbons are shown as white circles. Created with BioRender.com.

(F–M) Comparison of the abundance of individual metabolites derived from ^{13}C5-glutamine in different metabolic pathways between pimozide-treated and untreated U251 cells (mean ± SD, $n = 3$). Statistical significance was determined by unpaired Student's t test or one-way ANOVA with Dunnett's multiple comparisons adjustments. Metabolomics studies are repeated twice. Results represent one of two independent experiments. See also Figures S1 and S2.

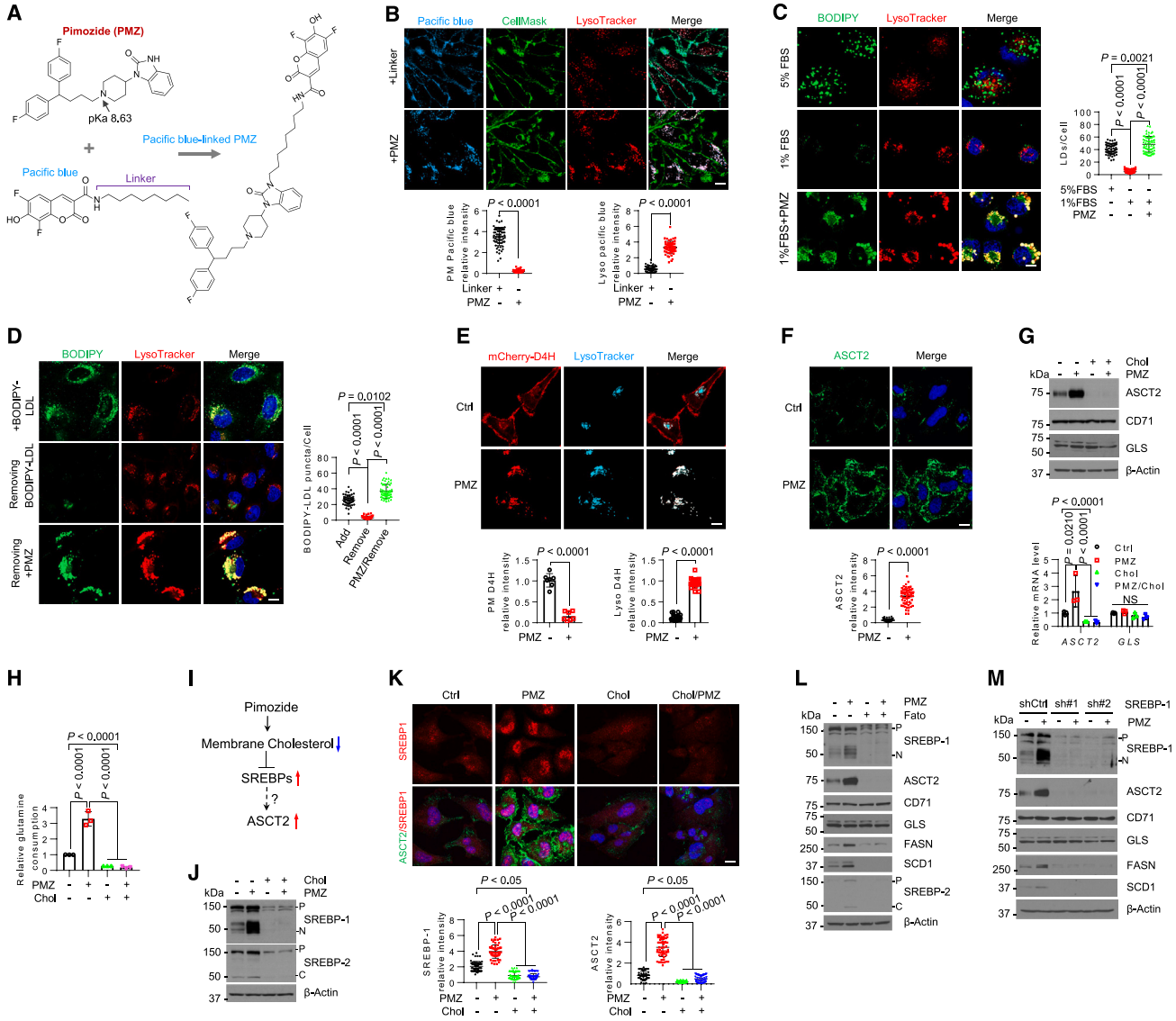

Figure 2. Pimozide acts via SREBP-1 to upregulate the expression of the glutamine transporter ASCT2 to promote glutamine consumption

(A) A schematic diagram illustrating the synthesis of Pacific blue-labeled pimozide. Created with ChemDraw.

(B) Representative fluorescence imaging of Pacific blue-labeled pimozide (3 μM) vs. Pacific blue with the linker only (3 μM) in U251 cells with co-staining of lysosomes by LysoTracker, plasma membrane by CellMask after treatment for 24 h in 1% FBS. Scale bar, 10 μm.

(C and D) Representative fluorescence images of lipid droplets (LDs) stained with BODIPY 493/503 (C) or BODIPY-labeled LDL (D) together with lysosome staining by LysoTracker in U251 cells after pimozide (3 μM) treatment for 24 h in 1%FBS. Scale bar, 10 μm.

(E) Representative fluorescence images of the cholesterol-binding probe derived from anaerobic bacteria *Perfringolysin O theta toxin* domain 4 (D4H) labeled by mCherry (GST-mCherry-D4H) in U251 cells under the same treatment as (C) and (D). The cells were co-stained with LysoTracker. Scale bar, 10 μm.

(F) Representative immunofluorescence images of anti-ASCT2 in U251 cells under the same treatment condition as (C) and (D). Nuclei were stained with DAPI. Scale bar, 10 μm.

(G) Western blotting analysis of membrane extracts (for ASCT2 and CD71) and total lysates (for GLS) (top) and real-time RT-PCR analysis of their gene expression (bottom) (mean ± SD, $n = 3$) in U251 cells after treatment with/without pimozide (3 μM) and cholesterol (3 μg/mL) for 24 h.

(H) Relative glutamine consumption levels in U251 cells after treatment as G and normalized with control cells (mean ± SD, $n = 3$).

(I) A schematic diagram illustrating the potential mechanism by which ASCT2 expression is upregulated by pimozide.

(J) Western blotting analysis of the total lysates of U251 cells after treatment as in panel G.

(K) Representative immunofluorescence images of anti-SREBP-1 and anti-ASCT2 in U251 cells after treatment as in (G). Scale bar, 10 μm.

(L and M) Western blotting analysis of U251 cells after treatment with/without pimozide (3 μM) and Fatostatin (Fato, 5 μM) for 24 h (L), or after shRNA silencing of SREBP-1 vs. shRNA control (shCtrl) for 48 h following treatment with or without pimozide (3 μM) for another 24 h in 1% FBS condition (M). P, precursor; N, N-terminal form; C, C-terminal form. See also Figures S3 and S4.

fluorescence reagent,[30] we found that pimozide treatment substantially increased lysosomal pH, evident in the shift from yellow (indicative of an acidic pH) to blue (indicating a more neutral pH) fluorescence signals (Figure S3F). Furthermore, through the utilization of DQ-Green BSA assays, we demonstrated that pimozide treatment markedly suppressed lysosomal hydrolytic activity, as indicated by a decrease in the bright green fluorescence observed in untreated cells (Figure S3G). We then delved into whether pimozide impeded the hydrolysis of lipid droplets (LDs) and low-density lipoprotein (LDL), both of which contain significant amounts of cholesteryl esters requiring lysosomal hydrolysis for the release of stored cholesterol and FAs to support GBM growth.[31–36] Notably, our fluorescence imaging experiments revealed that pimozide treatment hindered the hydrolysis of both LDs (Figure 2C) and LDL (Figure 2D), leading to their accumulation within the lysosomes.

We then proceeded to investigate whether pimozide treatment resulted in a reduction of membrane cholesterol. To assess this, we employed a fluorescence probe, GST-mCherry-D4H, derived from the anaerobic bacteria Perfringolysin O theta toxin domain 4 (D4H) (mCherry-D4H, red), which can detect membrane cholesterol levels when they exceed 20% of total membrane lipids.[31,37] In untreated GBM cells, we observed strong GST-mCherry-D4H binding in the plasma membrane, with modest binding to the lysosomes (Figure 2E). In contrast, in pimozide-treated cells, GST-mCherry-D4H fluorescence was exclusively observed within the lysosomes (Figure 2E), indicating a significant reduction in membrane cholesterol levels outside of the lysosomal compartments due to pimozide treatment.

Cholesterol reduction activates SREBP-1, leading to upregulation of ASCT2 expression and increased glutamine consumption

We subsequently investigated whether pimozide-induced membrane cholesterol reduction had a direct correlation with its stimulation of glutamine consumption. Through a combination of immunofluorescence (IF), western blotting, and real-time PCR analyses, we made the unexpected discovery that pimozide treatment led to a significant increase in both protein and mRNA levels of the glutamine transporter ASCT2, encoded by *SLC1A5* gene, but not glutaminase (GLS) (Figures 2F, 2G, and S4A–S4D). In addition, enzyme activity measurement showed that pimozide treatment did not affect GLS enzyme activity (Figure S4E). In contrast, the elevation in ASCT2/SLC1A5 expression correlated with heightened glutamine consumption under the same treatment conditions (Figure 2H). Importantly, these observed elevations in ASCT2/SLC1A5 expression and glutamine consumption disappeared when cholesterol was added to the cell culture medium (Figures 2G, 2H, and S4F–S4H).

We wondered whether sterol regulatory element-binding proteins (SREBPs), crucial lipogenic transcription factors whose activation is negatively regulated by cholesterol levels,[38–41] were involved in ASCT2 upregulation and glutamine uptake (Figure 2I). Through a combination of western blotting and IF imaging, we observed that pimozide treatment markedly promoted SREBP-1 cleavage and subsequent nuclear translocation—key indicators of SREBP activation (Figures 2J, 2K, S4F, and S4G).[34,40,42,43] This activation coincided with the upregulation of ASCT2 expression and its distribution to the plasma membrane (Figures 2F, 2G, 2K, S4F, and S4G). In contrast, SREBP-2 cleavage was only slightly increased by pimozide (Figures 2J and S5F). Notably, the supplementation of the culture medium with cholesterol completely abolished both SREBP-1 activation and ASCT2 upregulation (Figures 2J, 2K, S4F, and S4G). Intriguingly, pharmacological (using fatostatin) or genetic (via short hairpin RNA [shRNA]) inhibition of SREBP-1, but not SREBP-2, completely abolished pimozide-induced ASCT2 expression (Figures 2L, 2M, and S4I–S4K).

We then delved into whether SREBP-1 directly regulates ASCT2 expression. We proceeded to analyze *SLC1A5* gene promoter (which encodes ASCT2) using the online JASPAR resource, a database of transcription factor binding profiles,[44,45] and identified three potential sterol regulatory element (SRE) sites (Figure 3A, upper panel). Subsequently, through chromatin immunoprecipitation (ChIP) assays and real-time PCR analysis, we confirmed that SREBP-1 bound to these identified sites (Figure 3A). To further validate these findings, we cloned the *SLC1A5* gene promoter into a pGL3-luciferase promoter reporter vector. Luciferase activity assays revealed that the N-terminal isoform SREBP-1a exhibited the highest potency in stimulating *SLC1A5* promoter activity (Figure 3B). Consistently, by introducing N-terminal active forms of SREBPs into GBM cells via adenovirus-mediated expression, western blotting and IF showed that SREBP-1a expression exhibited the strongest upregulation of ASCT2 expression, while SREBP-1c had a modest effect, and SREBP-2 had minimal to no effect (Figures 3C, 3D, S5A, and S5B). Consistently, elevated glutamine consumption was observed in GBM cells expressing N-terminal SREBP-1a and -1c, with no significant effect in SREBP-2-expressing cells (Figures 3E and S5C).

Additionally, we conducted an extensive analysis of clinical samples through western blotting and immunohistochemistry (IHC). Our observations revealed a strong co-upregulation of SREBP-1 and ASCT2 in GBM tumor tissues, whereas both were expressed at lower levels in adjacent normal brain tissues (Figures 3F–3J and S5D–S5J; Table S1). This correlation was further corroborated by their higher mRNA expression levels in human GBM compared to normal brain tissues from TCGA (The Cancer Genome Atlas) and GTEx (The Genotype-Tissue Expression) database (Figure S5K). Interestingly, the expression of *SREBF2* gene was significantly lower in GBM compared to normal brain tissues, which contrasted with higher expression levels of *ASCT2* and *SREBP-1a* in GBM tissues (Figure S5K).

In summary, our data reveal that pimozide via activation of SREBP-1 upregulates ASCT2 expression and subsequent promotion of glutamine consumption in GBM cells.

Pimozide boosts SREBP-1-driven glutamine uptake in a feedforward loop to concurrently stimulate both glutamine metabolism and lipogenesis

We recently made the discovery that glutamine uptake and metabolism result in the intracellular release of ammonia that serves as a pivotal activator to stimulate SREBP-1 activation and subsequent lipogenesis.[46] Building upon this finding and our current results demonstrating SREBP-1 directly upregulates ASCT2 expression (Figures 2I–2M, 3A–3D, and S4E–S4J), we postulated the existence of a feedforward loop involving

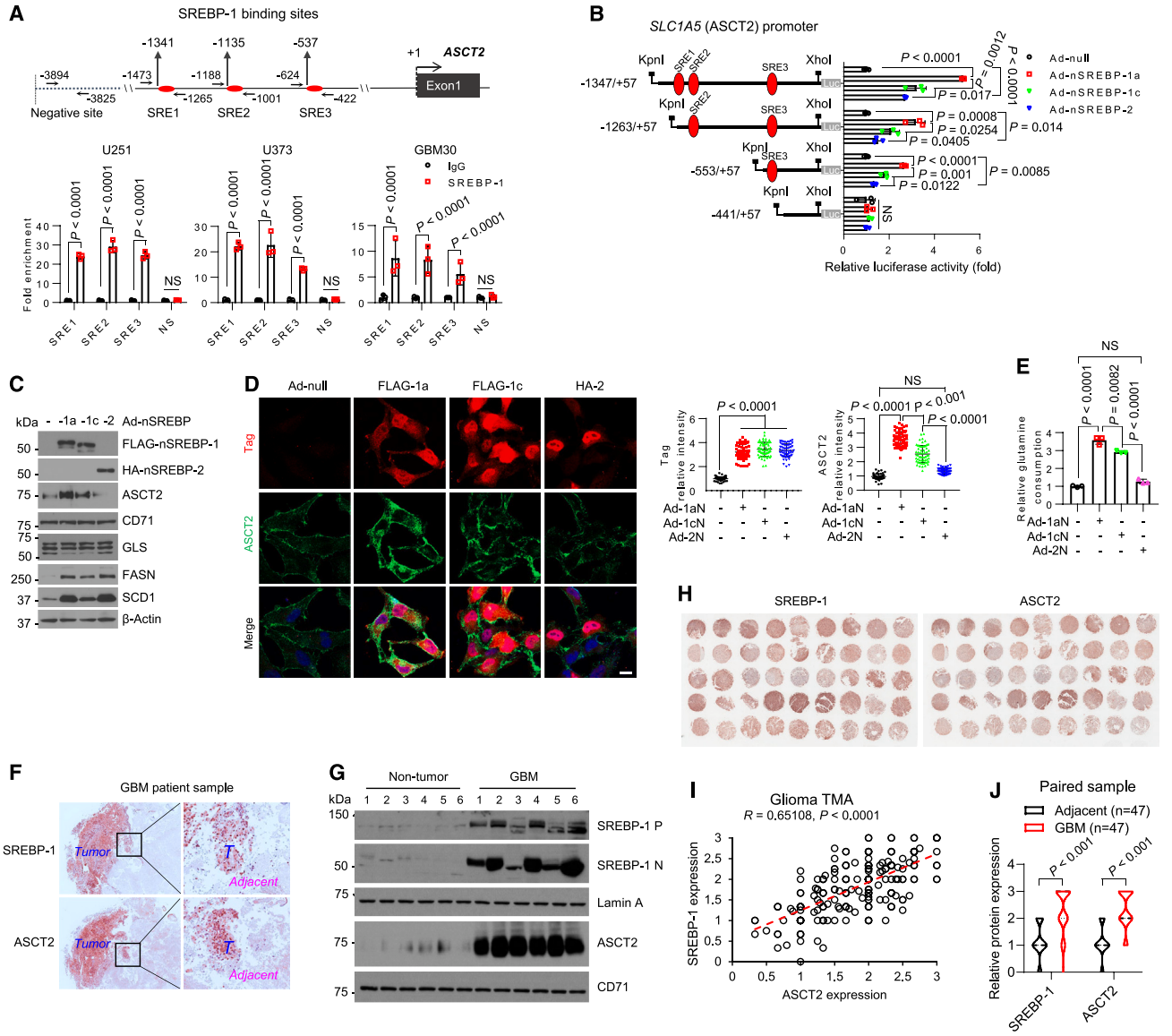

Figure 3. SREBP-1 transcriptionally activates SLC1A5 gene expression to promote glutamine consumption

(A) The putative SREBP-1 binding sites (SREs) and negative binding site (NS) in the SLC1A5 promoter (top). The arrows show the locations of the designed primers for PCR analysis after immunoglobulin G (IgG) or anti-SREBP-1 antibody-mediated chromatin immunoprecipitation (ChIP) (Bottom).

(B) A schematic diagram illustrating the cloning of different fragments of the SLC1A5 promoter in pGL3-luciferase (Luc) reporter plasmid (left) and measuring their activities in U251 cells in response to the expression of different N-terminal SREBP isoforms (right).

(C and D) Western blotting (C) and immunofluorescence (D) analysis of U251 cells after adenovirus (Ad)-mediated expression of FLAG- or hemagglutinin (HA)-labeled N-terminal SREBP-1a, -1c, or -2 isoforms for 48 h in 5% FBS condition. Scale bar, 10 μm.

(E) Relative glutamine consumption levels in U251 cells after expressing N-terminal SREBP isoforms as in (C) and normalized with control cells (Ad-null) (mean ± SD, $n = 3$).

(F) Immunohistochemistry (IHC) staining of human GBM tumor (T) vs. Adjacent brain tissues. Scale bars, 50 μm.

(G) Western blotting analysis of membrane and nucleus lysates of GBM tumor vs. non-tumor brain tissues from patient autopsies ($n = 6$).

(H–J) Representative images of IHC staining of SREBP-1 (left) and ASCT2 (right) (H) and scatterplots of their relative expression (I) in human glioma tissue microarray (TMA, $N = 223$). The expression levels of SREBP-1 and ASCT2 in paired GBM samples with adjacent brain tissues (J). Experiments from (A–D) were repeated three times. The results represent one of three independent experiments. Statistical significance for (A, B, D, E, and J) were determined by one-way ANOVA with Dunnett's multiple comparisons adjustments. See also Figure S5 and Table S1.

SREBP-1 activation, ASCT2 expression, glutamine uptake, and ammonia release (Figure 4A). To test this hypothesis, we initially examined human glioma samples using Nessler's staining to detect ammonia levels[47] and conducted IHC to evaluate protein levels. Our observations revealed elevated levels of ammonia, indicated by dark brown dots, in GBM tumor tissues (Figure S6A).

CellPress
OPEN ACCESS

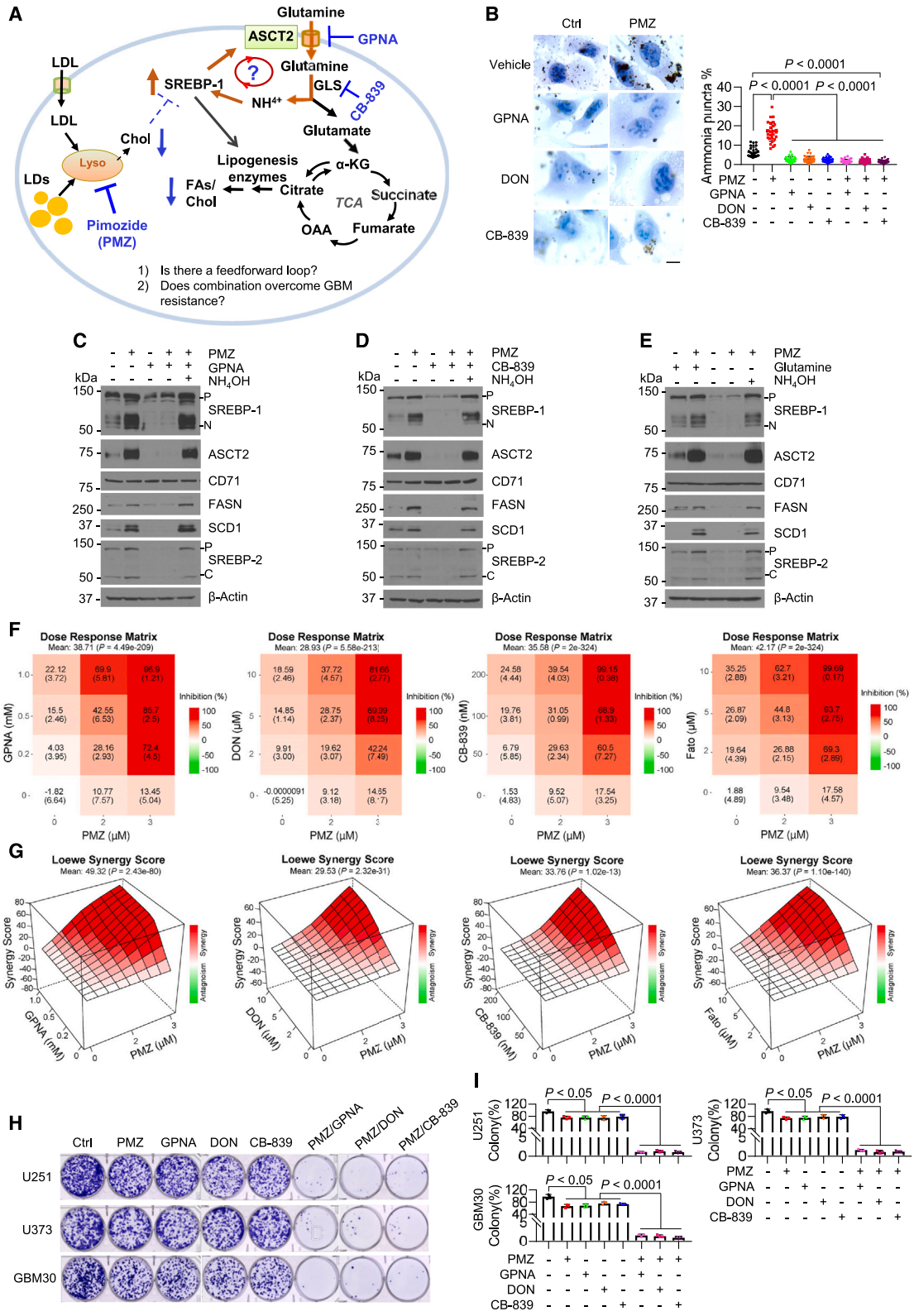

Figure 4. Pimozide activates SREBP-1/glutamine uptake feedforward loop that promotes GBM resistance

(A) This schematic diagram illustrates the proposed model of a potential feedforward loop activated by pimozide, leading to the development of GBM resistance. It also highlights the potential efficacy of pharmacological targeting of ASCT2 or GLS in combination with pimozide in effectively eliminating tumor cells.

(legend continued on next page)

This elevation in ammonia levels correlated with increased expression of SREBP-1 and ASCT2 when compared to normal brain and low-grade glioma tissues (Figure S6A). Furthermore, we analyzed tissues from healthy mice and found that ammonia levels in various mouse tissues were closely associated with the expression levels of SREBP-1, ASCT2, and GLS. They were all highly abundant in the small intestine, kidney, spleen, and muscle, modestly presented in the large intestine and liver, and displayed low levels in the brain and pancreatic tissues (Figure S6B).

To validate the existence of this feedforward loop, we investigated whether ammonia levels in GBM cells were elevated by pimozide (Figure 4A). Indeed, through Nessler's staining, we observed a significant increase in ammonia levels in pimozide-treated GBM cells compared to untreated cells (Figure 4B). This was accompanied by heightened SREBP-1 activation and increased ASCT2 expression (Figures 4C–4E and S7A–S7C, lane 2 vs. 1). In contrast, the inhibition of ASCT2 with L-γ-glutamyl-p-nitroanilide (GPNA), various glutamine utilization enzymes with 6-diazo-5-oxo-L-norleucine (DON), or GLS with CB-839 led to the abolishment of elevated ammonia levels, SREBP-1 activation, and ASCT2 expression, as well as the expression of the two key lipogenic enzymes fatty acid synthase (FASN) and stearoyl desaturase 1 (SCD1) (Figures 4B, 4D, S7A, and S7B, lane 4 vs. 2). However, the supplementation of ammonia solution (NH_4OH) in the presence of these inhibitors fully restored SREBP-1 activation and the levels of ASCT2, FASN, and SCD1 (Figures 4C and 4D, lane 5 vs. 4, and S7A and S7B, lane 5 vs. 4). Consistently, the removal of glutamine also abolished pimozide-induced SREBP-1 activation and ASCT2/FASN/SCD1 expression, all of which were restored by addition of ammonia (NH_4OH) (Figures 4E and S7C). Moreover, genetic inhibition of ASCT2 via shRNA-mediated knockdown reduced SREBP-1 activation and FASN/SCD1 expression in multiple GBM cells (Figure S7D). Finally, in an orthotopic xenograft model in mice, we found that knockdown of ASCT2 resulted in reduced levels of both ammonia and SREBP-1 in GBM tumor tissues, along with a significant inhibition of tumor growth and extension of overall survival (Figures S7E–S7H).

We next examined whether disrupting SREBP-1 activation/glutamine uptake feedforward loop by combining inhibition of glutamine metabolism and lysosomal function had synergistic inhibitory effects on GBM cells. To test this, we treated GBM cells with multiple doses of GPNA, DON, CB-839, or Fatostatin in combination with pimozide for 48 h. The analysis using online SynergyFinder web application showed the strong synergy for each drug combination with pimozide in inhibiting GBM cell viabilities (Figures 4F and 4G). Furthermore, the combination of GPNA, DON, or CB-839 with pimozide resulted in the nearly complete eradication of pre-formed GBM cell colonies and the death of these cells, while each drug alone exhibited only a marginal inhibitory effect at the same dose (Figures 4H, 4I, and S8A). In contrast, these treatments did not significantly affect normal human astrocytes (NHAs) (Figure S8A).

In conclusion, our data reveal SREBP-1 activation/ASCT2 expression/glutamine uptake/ammonia release feedforward loop, which is upregulated by pimozide to promote GBM cell resistance (Figure 4A).

Inhibiting glutamine consumption synergizes with pimozide to induce mitochondrial damage and oxidative stress to blunt GBM cell growth

Strikingly, transmission electron microscopy (TEM) imaging revealed that the mitochondria in GBM cells subjected to the combination treatments of GPNA, DON, and CB-839 with pimozide were dramatically fragmented and displayed a loss of cristae, in stark contrast to the slight effects observed with each drug alone, when compared to control cells (Figures 5A and 5B). Fluorescent imaging using MitoTracker or EGFP-OMP25, a GFP-labeled mitochondrial outer membrane protein,[48] confirmed extensive mitochondrial fragmentation in GBM cells following combination treatments, in contrast to single-drug treatment and control cells (Figures 5C and S8B–S8D). The combinations also led to a substantial reduction in mitochondrial membrane potential (Figure S8E).

We then investigated whether mitochondrial damage resulted in elevated levels of oxidative stress, leading to the death of GBM cells. Our findings confirmed that the combination of pimozide with GPNA, DON, or CB-839 all led to a significant increase in reactive oxygen species (ROS) within mitochondria, as indicated by CellROX staining (red) together with MitoTracker staining (green), while single-drug treatments only induced a modest rise in ROS levels (Figures 5C, S8C and S8D). These combinations also caused a substantial reduction in mitochondrial oxygen consumption rate (OCR) (Figure 5D), along with increased levels of apoptotic markers such as cleaved caspase-3, -6, and poly-ADP ribose polymerase (PARP) (Figures 5E and S8F). In contrast, supplementation with GSH in these cells markedly reduced the ROS induced by the drug combination, restored mitochondrial morphology to a tubular and elongated structure like untreated cells (Figures 5F, S9A, and S9B), prevented the release of cytochrome *c* from the mitochondria into the cytosol, inhibited apoptotic marker cleavage, and rescued GBM cells from death (Figures 5G, S9C, and S9D).

(B) Nessler's staining of ammonia (dark brown dots) in U251 cells after treatment with or without pimozide (3 μM), GPNA (1 mM), CB-839 (100 nM), or DON (10 μM) alone or combination for 24 h in 1% FBS. Ammonia dots were quantified by ImageJ from 30 cells (mean ± SD) and normalized with total cell areas (right). Scale bar, 100 μm.

(C–E) Western blotting analysis of U251 cells under the same treatment condition as in (B) in the presence or absence of glutamine (4mM) (E) or ammonia solution (NH4OH) (4 mM).

(F) Combination treatment effects of pimozide (PMZ) with GPNA, DON, CB-839, or Fatostatin (Fato) at indicated doses (48 h) on GBM U251 cell viabilities. Values in each block represent the mean cell viability inhibition with SD (n = 3).

(G) Three-dimensional (3D) plot showing the Loewe synergy score of pairwise dose combinations as shown in (F) in U251 cells. z axis, synergy score; x/y axis, drug combination with different doses.

(H and I) Effects of drug treatment as in B for 8 days on GBM cells-derived colonies in 1% FBS (H). Colony numbers were quantified by ImageJ and normalized with untreated cells (I). See also Figures S6 and S7.

CellPress
OPEN ACCESS

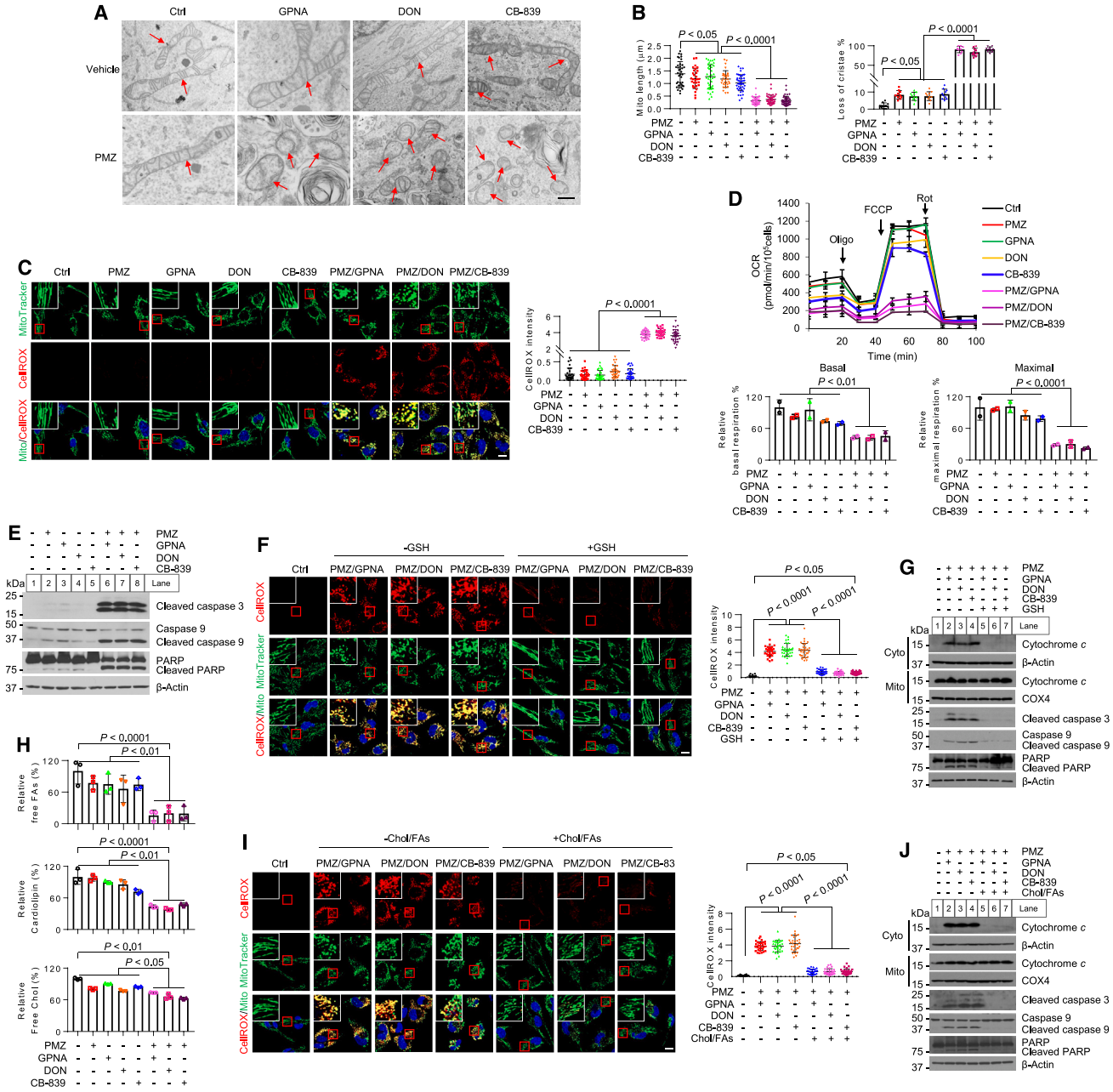

Figure 5. Inhibition of glutamine consumption synergizes with pimozide to induce mitochondrial damage and oxidative stress that blunts GBM cell growth

(A and B) Representative transmission electron microscopy (TEM) images of the mitochondria in U251 cells after treatment (A). Scale bar, 500 nm. Red arrows indicate mitochondria. Over 30 mitochondria were quantified (mean ± SEM) (B).

(C) Representative fluorescence images of U251 cells stained with MitoTracker and CellROX Deep Red after treatment as (A). CellROX-positive signals were quantified by ImageJ in more than 30 cells (mean ± SEM) (right). Scale bar, 10 μm.

(D) Oxygen consumption rate (OCR) measured by Seahorse XF24 in U251 cells after treatment as (A) (top, mean ± SD, $n = 3$). Oligo, oligomycin; FCCP, carbonyl cyanide 4-trifluoromethoxy-phenylhydrazone; Rot, rotenone. Relative basal and maximal respiration was normalized with the untreated control cells (bottom).

(E) Western blotting analysis of U251 cells after treatment as in (A) for 48 h.

(F) Representative fluorescence images of U251 cells stained with MtioTracker and CellROX Deep Red after treatment as in (A) in the presence or absence of GSH (3 mM) for 24 h. Scale bar, 10 μm. CellROX-positive signals were quantified by ImageJ in over 30 cells (mean ± SEM) (right). Scale bar, 10 μm.

(G) Western blotting analysis of the cytosol (Cyto), mitochondrial (Mito), and total lysates of U251 cells after treatment as in (A) for 48 h.

(H) Relative free FA, cardiolipin, and free cholesterol levels in U251 cells after treatment as in (A).

(legend continued on next page)

Pimozide, as shown in Figures 2C and 2D, inhibits the release of cholesterol and FAs from LDs and LDL hydrolysis. On the other hand, the inhibition of glutamine consumption reduces *de novo* lipid synthesis by suppressing SREBP-1 activity, as demonstrated in Figures 4A–4E and S7A–S7D. We then investigated whether combining pimozide with inhibitors of glutamine consumption significantly reduced cellular cholesterol and FA levels, resulting in synergistic effects in killing GBM cells. Indeed, the combination of pimozide with GPNA, DON, or CB-839 all led to a marked reduction in levels of free FAs, cardiolipin, and free cholesterol (Figure 5H). Supplementation with cholesterol and FAs (a mixture of palmitate 16:0, palmitoleic acid 16:1, and oleic acid 18:1) significantly attenuated the ROS levels induced by the combination treatments (Figures 5I and S9E), restored mitochondrial morphology to a state resembling untreated cells (Figures 5I and S9E), and reduced cytochrome *c* release and caspases-3/9 and PARP cleavage (Figures 5J and S9F), ultimately rescuing GBM cells from the combination-induced cell death (Figure S9G).

Combining glutamine consumption inhibition with pimozide effectively suppresses GBM growth *in vivo*

We next assessed the initial efficacy of pimozide in a primary GBM30 cells-derived subcutaneous xenograft mouse model. Pimozide treatment showed only marginal inhibition of tumor growth (Figures S10A–S10C). Through IHC and Nessler's staining analyses, we observed that pimozide treatment significantly increased SREBP-1, ASCT2, ammonia, and FASN levels in tumor tissues from pimozide-treated mice tumors as compared to control tumors (Figure S10D). We then investigated whether pharmacological inhibition of ASCT2 with GPNA or inhibition of GLS with CB-839 could sensitize GBM tumor to pimozide treatment. Strikingly, the combination of either GPNA or CB-839 with pimozide demonstrated a powerful synergistic antitumor effect in this subcutaneous xenograft model (Figures 6A and 6B). We further tested the effects of combining the SREBP-1 inhibitor fatostatin with pimozide in GBM cells and found that they synergistically damaged mitochondria, increased ROS (Figures S11A and S11B), reduced mitochondria membrane potential (Figures S11C and S11D), triggered apoptosis (Figure S11E), and eradicated GBM cells preformed colonies and effectively killed GBM cells *in vitro* (Figures S11F and S11G). Importantly, in an *in vivo* xenograft model, this combination therapy also synergistically inhibited GBM growth (Figures 6C and 6D). Encouragingly, examination via H&E staining did not reveal obvious toxic effects in vital organs such as the kidney, liver, pancreas, spleen, brain, small intestine, and lager intestine after drug treatment of the mice (Figures S12A–S12G). These findings suggest the potential clinical promise of this combination therapy in the treatment of GBM.

We next examined three GBM patient-derived organoids to validate the efficacy of our proposed therapy. Notably, organoids have been recognized as a more physiologically relevant model of human cancer, including GBM, as it sustains human tumor microenvironment.[49] Clearly, our results showed that combining pimozide with GPNA, DON, CB-839, or fatostatin dramatically induced tumor cell death (propidium iodide, PI staining) (Figure 6F) and significantly reduced organoid size and inhibited tumor cell viability (Figure 6G) in all GBM patient-derived organoids.

We further determined the antitumor effects of the combination of pimozide with GPNA, CB-839, or fatostatin in intracranial GBM mouse models, in both female and male mice, by using primary GBM cells (GBM30) derived from a female patient (Figure 7A). By magnetic resonance imaging (MRI) conducted on day 12 after drug treatments, we found that all combinations significantly inhibited GBM tumor growth in the mouse brain of female mice compared to the control and single-drug treatment groups (Figures 7B, S12H, and S12I). Kaplan-Meier plot analysis demonstrated that all the combinations significantly extended the overall survival of GBM-bearing mice compared to the control and single-drug treatment groups, and there was no obvious difference in response between female and male mice (Figures 7C and 7D). Through IHC and ammonia staining, we observed that pimozide treatment significantly increased SREBP-1, ASCT2, ammonia, and FASN levels in intracranial tumor tissues (Figure 7E). Importantly, these increases were effectively reversed by combining pimozide with GPNA, CB-839, or fatostatin (Figure 7E). IHC analysis further revealed that these combinations significantly reduced Ki67 staining, a marker of cell proliferation, while there were marked increase in cleaved caspase-3 levels in the tumor tissues (Figure 7E). Moreover, these combinations significantly increased the therapeutic effects of radiation on GBM growth, effectively suppressing intracranial tumor growth and extending the survival of female mice bearing GBM (Figures 7F–7H). We also measured mouse blood ammonia levels following drug treatments. Interestingly, ammonia levels in mouse blood were significantly increased approximately 1.5-fold in pimozide-treated mice compared with control mice without drug treatment, which were restored to the basal levels as those of control mice when combined with GPNA, CB-839, or fatostatin treatments (Figure S12J).

DISCUSSION

A major obstacle in effectively treating GBM is the development of tumor resistance to nearly all current treatments.[1,2] Therefore, understanding the underlying mechanisms of this resistance is crucial for the development of successful GBM therapy. Antipsychotic drugs have long been studied for their potential antitumor properties.[4,10,50] However, their translation into clinical cancer therapy has been hampered by issues of tumor resistance, despite the proposal of various antitumor mechanisms for this

(I) Representative fluorescence images of U251 cells stained with MitoTracker and CellROX Deep Red after treatment as in (A) in the presence or absence of the mixture of cholesterol (3 μg/mL) and FAs (palmitate: 20 μM, oleic acid: 20 μM, palmitoleic acid: 5 μM). CellROX-positive signals were quantified by ImageJ in over 30 cells (mean ± SEM) (right). Scale bar, 10 μm.

(J) Western blotting analysis of U251 cells after treatment as in (A) for 48 h. Experiments except TEM (A, twice) were repeated three times. The results were representatives of one of three (two) independent experiments. Statistical significance for all the results was determined by one-way ANOVA with Dunnett's multiple comparisons adjustments. See also Figures S8 and S9.

CellPress
OPEN ACCESS

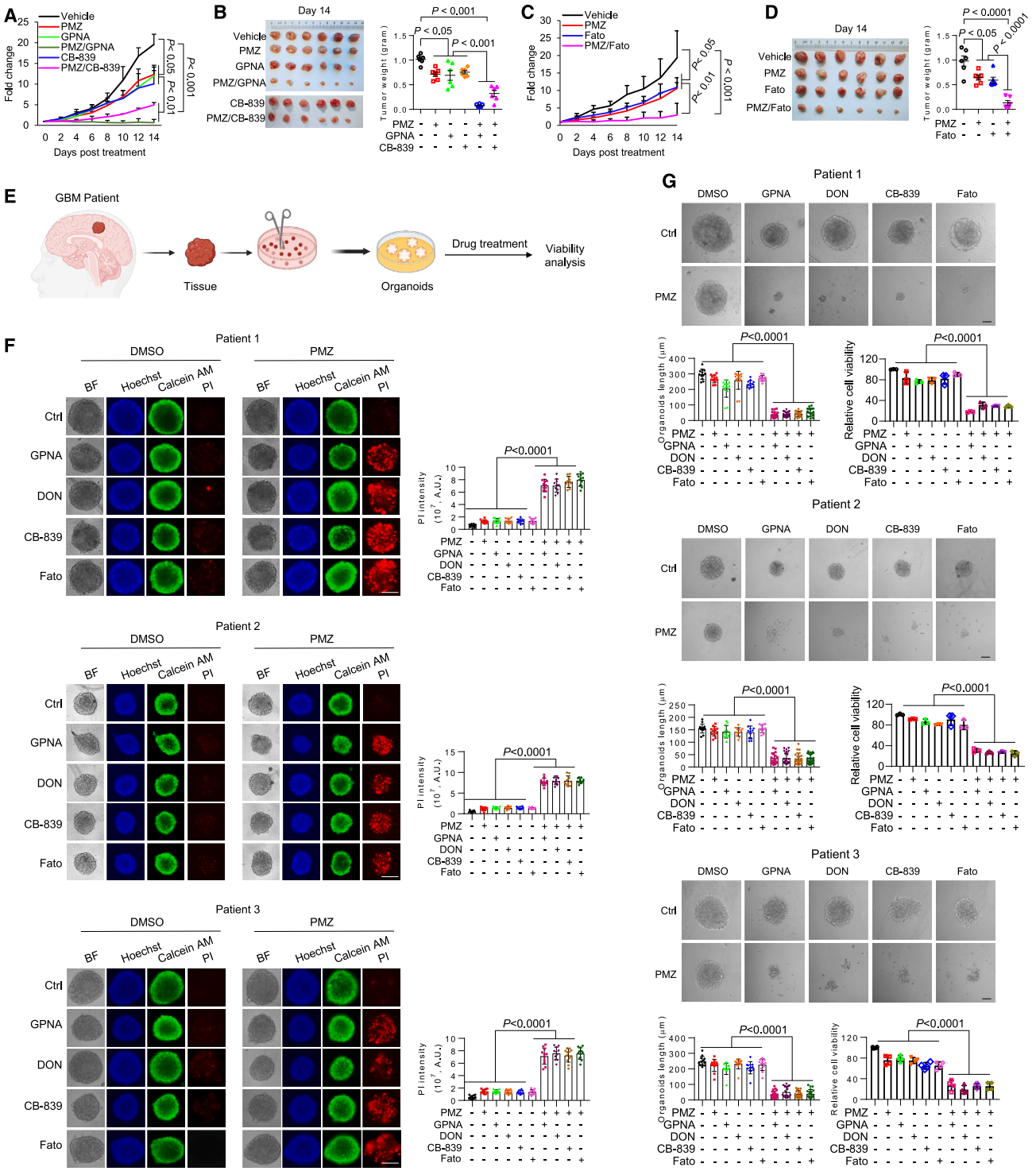

Figure 6. Combining an inhibitor of glutamine uptake or its consumption with pimozide synergistically suppresses tumor growth in GBM xenografts and patient-derived organoids

(A–D) Tumor growth curve of GBM30-derived subcutaneous xenografts (n = 6, mean ± SD) treated with pimozide (15 mg/kg/day, intraperitoneal [i.p.]) in combination with or without GPNA (60 mg/kg/day, i.p.), CB-839 (20 mg/kg/day, i.p.) (A), or Fatostatin (20 mg/kg/day, i.p.) (C) for 14 days. Tumors were imaged after 14 days treatment and weighed (B and D).

(E) Schematic diagram illustrating the development of GBM patient-derived organoids for drug treatment. Created with BioRender.com.

(legend continued on next page)

large class of drugs.[6,21] This aspect has received limited attention in previous research. Our study sheds light on a mechanism of resistance to the antipsychotic drug pimozide in GBM.

Metabolic plasticity empowers GBM resistance to lysosome inhibition

Our findings reveal that pimozide activates a feedforward loop involving SREBP-1 activation and increased glutamine uptake, which ultimately promotes GBM resistance to therapy (Figure S13). Additionally, our study highlights the remarkable adaptability of GBM cells in response to lysosome inhibition, demonstrating their ability to switch between metabolic pathways to ensure survival. Specifically, when one metabolic resource, such as cholesterol and FAs, is limited due to the inhibition of lysosomal hydrolysis, GBM cells can compensate by upregulating an alternative pathway, namely glutamine uptake and reductive carboxylation-mediated *de novo* lipid synthesis, to replenish these crucial building blocks (Figure S13). This metabolic switch identified in our study has important implications for the development of combination therapies to counteract this adaptive response and improve treatment outcomes in GBM. Overall, our research opens possibilities for understanding and overcoming resistance mechanisms in GBM and potentially in other cancers. It emphasizes the importance of metabolic adaptability in cancer cells and highlights the potential of combination therapies to address this challenge.

Unexpected role of SREBP-1 in regulating glutamine metabolism

The discovery of SREBP-1's role in regulating glutamine metabolism shifts the conventional thoughts regarding the functions of SREBPs. For over three decades, SREBPs have been thought mainly to regulate cholesterol and FA biosynthesis.[38] However, our study demonstrates that SREBP-1 has a role in governing glutamine metabolism. The identification of the feedforward loop involving SREBP-1, ASCT2, glutamine uptake, and ammonia release provides a comprehensive review of how SREBP-1 can orchestrate two critical metabolic pathways simultaneously: lipid synthesis and glutamine consumption (Figure S13). Moreover, our recent discovery that ammonia released by glutamine catabolism can activate SREBP cleavage and nuclear translocation[46] further underscores the intricate connections between metabolic pathways and transcriptional regulation. These insights stand to impact not only cancer research but also our broader understanding of metabolic regulation in health and disease.

Combining glutamine metabolism and lysosome inhibition is an effective strategy targeting cancers

The combination of targeting glutamine metabolism via ASCT2 or GLS inhibition along with pimozide represents a promising strategy to broadly inhibit glutamine's functions, limit lipid supplies for tumor cells, and effectively kill GBM cells, as illustrated in Figure S13. However, as mentioned, targeting GLS alone has shown limited success in clinical trials,[51] a trend that aligns with our study's findings indicating that CB-839 alone is insufficient to restrain tumor growth in an intracranial GBM model. Many clinical trials have explored the use of CB-839 in combination with various anticancer agents, such as chemotherapeutics, molecule target inhibitors, and immune checkpoint inhibitors. But these combinations often lack clear mechanistic synergies and have not yielded promising results. In contrast, the synergistic combination of CB-839 with pimozide, as supported by our research, provides a rational and mechanistically driven approach (Figure S13). Moving this combination to clinical trials could hold promise for improving GBM therapy if successful.

Critical role of cholesterol and FAs in preserving mitochondrial integrity and function

Cholesterol and FAs are essential lipids for cell function.[31,52–54] Maintaining an adequate supply of these lipids is essential for supporting cell proliferation. Despite this knowledge, the precise mechanism underlying tumor cell death due to lipid deficiency has remained elusive. Our study brings to light the fact that mitochondria are particularly susceptible when confronted with a shortage of cholesterol and FAs. Consequently, when we inhibit lipid synthesis and the release of lipids from LDs and LDL through a combination of inhibiting glutamine uptake or consumption and targeting lysosomal function, it leads to severe mitochondrial damage and a surge in oxidative stress. These factors collectively lead to apoptotic cell death in GBM. Our findings provide insights into the pivotal role of mitochondria in responding to lipid deficiencies, offering valuable implications for potential therapeutic strategies not only for GBM but also for other cancers.

Limitations of the study

Though the combination of glutamine metabolism inhibitors with pimozide showed significant antitumor effects, the orthotopic GBM-bearing mice still died around approximately 40 days. We think the main reason for GBM-bearing mice maintaining resistance to the combination treatments is that the BBB limits the effective drug doses in the brain, leading to residual tumor growth and mouse death. This reasoning is supported by the results of the efficacy of drug treatments in the GBM subcutaneous tumor model. In that model, each single drug showed a modest antitumor effect, while the single-drug treatments did not show significant antitumor effects in the orthotopic model. This is a common issue for drug treatment in brain tumors. In a future study, we need to utilize a strategy, such as localized ultrasound, to further increase

(F) Representative imaging of GBM organoids derived from 3 patients stained with Hoechst33342 (blue, nuclei), Calcein-AM (green, live cells), and propidium iodide (PI, red, dead cells) after treatment with pimozide (PMZ, 3 μM), GPNA (1 mM), DON (10 μM), CB-839 (100 nM), or Fatostatin (Fato, 5 μM) alone or combination for 3 days. BF, bright field. PI intensity was quantified by ImageJ in ≥10 organoids derived from each patient (mean ± SD).
(G) Representative bright-field images (top), size, and viabilities (bottom) of GBM organoids after treatments as (F) for 10 days. The maximum length of organoids was measured by ImageJ (size). Viabilities of organoids were measured by CellTiter-Glo luminescent cell viability assay. Biological statistic for all the results in Figure 6 was examined by one-way ANOVA with Dunnett's multiple comparisons adjustments. See also Figures S10–S12.

CellPress
OPEN ACCESS

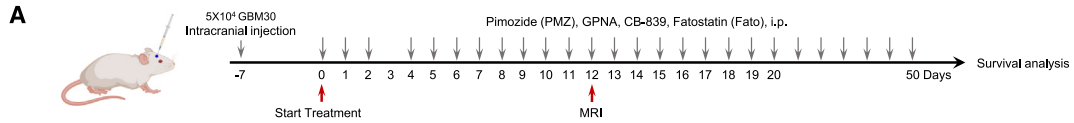

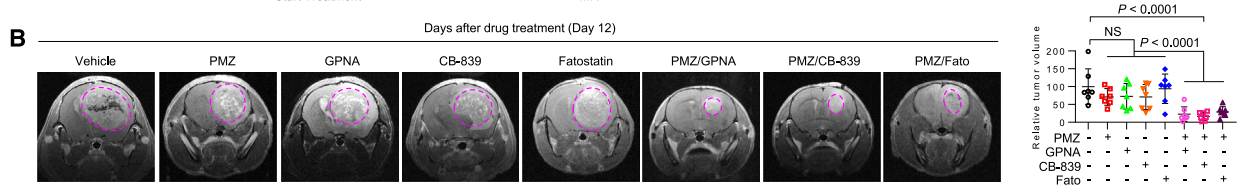

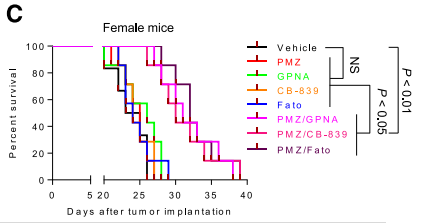

	Vehicle	PMZ	GPNA	CB-839	Fato	PMZ/GPNA	PMZ/CB-839	PMZ/Fato
Median survival (days)	24	25	26	24	24	31	30	32

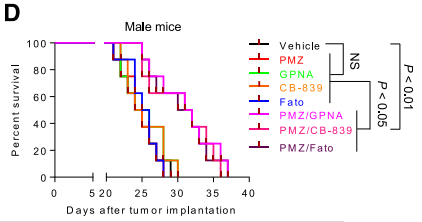

	Vehicle	PMZ	GPNA	CB-839	Fato	PMZ/GPNA	PMZ/CB-839	PMZ/Fato
Median survival (days)	24	24.5	25	24.5	25.5	31.5	31.5	31

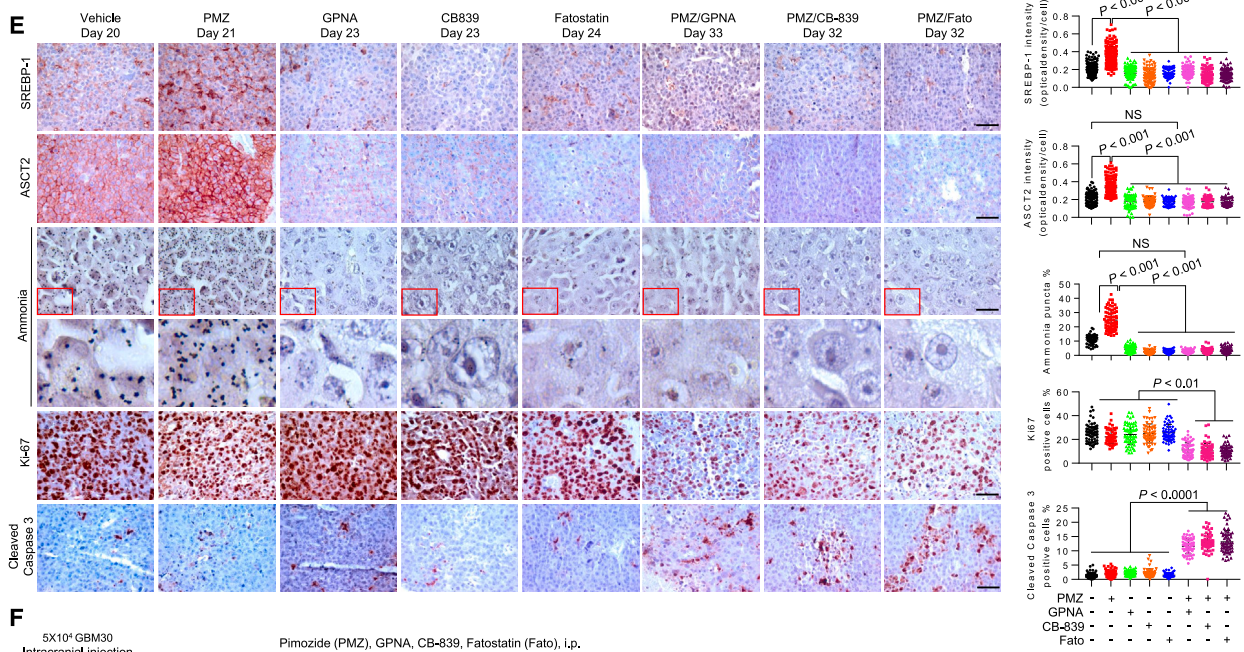

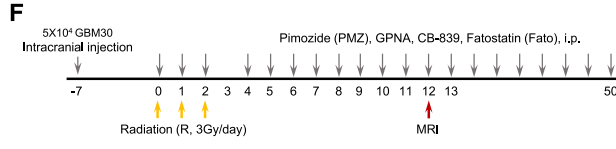

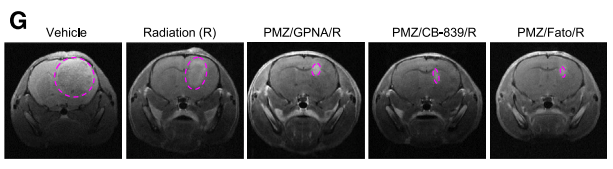

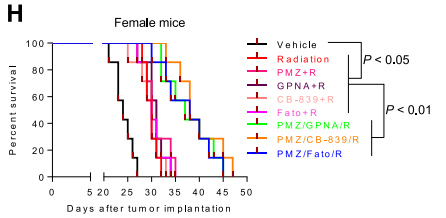

	Vehicle	R	PMZ/R	GPNA/R	CB-839/R	Fato/R	PMZ/GPNA/R	PMZ/CB-839/R	PMZ/Fato/R
Median survival (days)	24	30	30	31	31	30	37	38	38

(legend on next page)

drug penetration into GBM tissues to completely eradicate tumor cells. The intracerebral drug levels should also be measured, providing insights for future clinical tests. Additionally, despite the likelihood of the aforementioned explanation, we cannot exclude the involvement of glycolysis and pyruvate carboxylation-mediated anaplerosis in tumor resistance. We also cannot exclude the possibility of drug efflux by efflux transporters, leading to the insufficient drug concentrations in GBM tissues. These possibilities should be tested in follow-up studies.

RESOURCE AVAILABILITY

Lead contact

Further information and requests for resources and reagents should be directed and will be fulfilled by the lead contact, Deliang Guo (deliang.guo@osumc.edu).

Materials availability

All plasmids and cell lines generated in this study are available from the lead contact with a completed materials transfer agreement.

Data and code availability

- All the data reported in this paper are available from the lead contact upon request.
- This paper does not report original code.
- Any additional information required to reanalyze the data reported in this paper is available from the lead contact upon request.

ACKNOWLEDGMENTS

This work was supported by NINDS and NCI (USA) grants NS104332, NS112935, NS141312, and CA240726 to D.G. and CA227874 to D.G. and A.C. We also appreciate the support from the OSUCCC-Pelotonia Idea grant and Urban and Shelly Meyer Fund for Cancer Research to D.G. MRI imaging was taken from the OSU Small Animal Imaging Core (SAIC) that is supported by the grant P30 CA016058.

AUTHOR CONTRIBUTIONS

D.G. conceived the ideas and led the project. Y.Z. and D.G. designed the experiments. Y.Z., F.G., and L.M. performed the experiments and analyzed data. X.Y., L.H., and X.Z. performed metabolomics study and analysis. S.M., E.X., P.-K.L., and X.C. synthesized fluorescence-labeled pimozide. A.P.B. and A.C. prepared glioma TMA. E.L. constructed ASCT2/*SLC1A5* gene promoter. H.S., Y.F., Y.K., C.-Y.C., Y.G., and Q.W. helped in animal studies. X.M. helped with heatmap and statistical analysis. Y.Z. and D.G. wrote the manuscript. We also thank Xipeng Ma from the University of Louisville for helping upload the metabolomics data to the National Metabolomics Data Repository (NMDR), the Metabolomics Workbench. All authors reviewed and approved the manuscript for publication.

DECLARATION OF INTERESTS

The authors declare no competing interests.

STAR★METHODS

Detailed methods are provided in the online version of this paper and include the following:

- KEY RESOURCES TABLE
- EXPERIMENTAL MODEL AND STUDY PARTICIPANT DETAILS
  - Cell lines and culture
  - Clinical samples
  - Intracranial and subcutaneous xenograft models
  - Organoid culture
- METHOD DETAILS
  - Synergy prediction
  - Colony growth assay
  - Stable isotope $^{13}C_5$-glutamine labeling, polar metabolite and long chain fatty acid sample preparation
  - LC-MS analysis and data processing
  - Synthesis of Pacific blue-labeled pimozide
  - Cell proliferation
  - Sphere formation assay
  - Preparation of Cell membrane fractions
  - Mitochondria and cytosol Fractionation
  - Western blotting
  - Quantitative real-time PCR
  - Lysosomal pH measurements
  - Lysosome activity
  - Lipid droplets (LDs) staining and quantification
  - Low-density lipoprotein (LDL) uptake and quantification
  - Chromatin immunoprecipitations (ChIP)
  - Promoter luciferase report assay
  - Production and infection of Lentivirus-shRNA
  - Immunofluorescence (IF)
  - Mitochondrial membrane potential (MMP)
  - Transmission electronic microscopy
  - Seahorse analysis
  - Detection of reactive oxygen species (ROS)
  - Free fatty acid measurement
  - Cardiolipin measurement
  - Cholesterol measurement
  - Glutaminase (GLS) activity measurement
  - Magnetic resonance imaging (MRI)
  - Hematoxylin and eosin (H&E) staining

Figure 7. Combining inhibition of glutamine metabolism with pimozide significantly suppresses tumor growth in orthotopic GBM models

(A) A schematic diagram outlining the treatment schedule for a GBM30-derived orthotopic xenograft model by pimozide (25 mg/kg/day, intraperitoneal [i.p.]), GPNA (60 mg/kg/day, i.p.), CB-839 (20 mg/kg/day, i.p.), or Fatostatin (20 mg/kg/day, i.p.) alone or in combination.

(B) Representative magnetic resonance imaging (MRI) of female mouse brains from the GBM30-derived orthotopic models after treatment as outlined in (A) for 12 days. The tumor border was outlined by a pink circle (left). Tumor volume was quantified by ITK-SNAP (Version 3.8.0) (right).

(C and D) Kaplan-Meier plot analysis of overall survival in GBM-bearing mice, in both female and male mice (n = 7/each sex) after treatment as outlined in (A). Significance was determined by a log rank test. NS, not significant.

(E) Representative IHC (proteins) and Nessler's (ammonia, dark brown dots) staining images of the intracranial GBM30-derived tumors isolated from the mice at the indicated days (endpoint) after treatment as outlined in (A). Six separate areas from each tumor were quantified by ImageJ (mean ± SEM, n > 1,000 cells) (right). Scale bars, 50 μm for IHC. 100 μm for ammonia staining.

(F–H) A schematic diagram outlining the treatment schedule for a GBM30-derived orthotopic xenograft model (female) by pimozide, GPNA, CB-839, or Fatostatin alone or in combination with radiation (F). Representative MRI images of mouse brains from the GBM30-derived orthotopic models (n = 7) after treatment for 12 days (G). Mouse overall survival was analyzed by Kaplan-Meier plot (H). Significance was determined by a Log rank test. Statistical significance from (B–G) was determined by one-way ANOVA with Dunnett's multiple comparisons adjustments. See also Figures S12 and S13.

SUPPLEMENTAL INFORMATION

Supplemental information can be found online at https://doi.org/10.1016/j.xcrm.2024.101706.

Received: December 8, 2023
Revised: June 7, 2024
Accepted: August 8, 2024
Published: September 4, 2024

REFERENCES

1. Cloughesy, T.F., Cavenee, W.K., and Mischel, P.S. (2014). Glioblastoma: from molecular pathology to targeted treatment. Annu. Rev. Pathol. *9*, 1–25. https://doi.org/10.1146/annurev-pathol-011110-130324.
2. Bagley, S.J., Kothari, S., Rahman, R., Lee, E.Q., Dunn, G.P., Galanis, E., Chang, S.M., Nabors, L.B., Ahluwalia, M.S., Stupp, R., et al. (2022). Glioblastoma Clinical Trials: Current Landscape and Opportunities for Improvement. Clin. Cancer Res. *28*, 594–602. https://doi.org/10.1158/1078-0432.CCR-21-2750.
3. Horbinski, C., Berger, T., Packer, R.J., and Wen, P.Y. (2022). Clinical implications of the 2021 edition of the WHO classification of central nervous system tumours. Nat. Rev. Neurol. *18*, 515–529. https://doi.org/10.1038/s41582-022-00679-w.
4. Matteoni, S., Matarrese, P., Ascione, B., Buccarelli, M., Ricci-Vitiani, L., Pallini, R., Villani, V., Pace, A., Paggi, M.G., and Abbruzzese, C. (2021). Anticancer Properties of the Antipsychotic Drug Chlorpromazine and Its Synergism With Temozolomide in Restraining Human Glioblastoma Proliferation In Vitro. Front. Oncol. *11*, 635472. https://doi.org/10.3389/fonc.2021.635472.
5. Aras, Y., Erguven, M., Aktas, E., Yazihan, N., and Bilir, A. (2016). Antagonist activity of the antipsychotic drug lithium chloride and the antileukemic drug imatinib mesylate during glioblastoma treatment in vitro. Neurol. Res. *38*, 766–774. https://doi.org/10.1080/01616412.2016.1203096.
6. Lee, J.K., Chang, N., Yoon, Y., Yang, H., Cho, H., Kim, E., Shin, Y., Kang, W., Oh, Y.T., Mun, G.I., et al. (2016). USP1 targeting impedes GBM growth by inhibiting stem cell maintenance and radioresistance. Neuro Oncol. *18*, 37–47. https://doi.org/10.1093/neuonc/nov091.
7. Squatrito, M., and Holland, E.C. (2011). DNA damage response and growth factor signaling pathways in gliomagenesis and therapeutic resistance. Cancer Res. *71*, 5945–5949. https://doi.org/10.1158/0008-5472.CAN-11-1245.
8. Chinot, O.L., Wick, W., Mason, W., Henriksson, R., Saran, F., Nishikawa, R., Carpentier, A.F., Hoang-Xuan, K., Kavan, P., Cernea, D., et al. (2014). Bevacizumab plus radiotherapy-temozolomide for newly diagnosed glioblastoma. N. Engl. J. Med. *370*, 709–722. https://doi.org/10.1056/NEJMoa1308345.
9. Cloughesy, T.F., and Mischel, P.S. (2011). New strategies in the molecular targeting of glioblastoma: how do you hit a moving target? Clin. Cancer Res. *17*, 6–11. https://doi.org/10.1158/1078-0432.CCR-09-2268.
10. Hsieh, Y.H., Chan, H.L., Lin, C.F., Liang, S.H.Y., Lu, M.L., McIntyre, R.S., Lee, Y., Lin, T.C., Chiu, W.C., and Chen, V.C.H. (2019). Antipsychotic use is inversely associated with gastric cancer risk: A nationwide population-based nested case-control study. Cancer Med. *8*, 4484–4496. https://doi.org/10.1002/cam4.2329.
11. Huang, J., Zhao, D., Liu, Z., and Liu, F. (2018). Repurposing psychiatric drugs as anti-cancer agents. Cancer Lett. *419*, 257–265. https://doi.org/10.1016/j.canlet.2018.01.058.
12. Shaw, V., Srivastava, S., and Srivastava, S.K. (2021). Repurposing antipsychotics of the diphenylbutylpiperidine class for cancer therapy. Semin. Cancer Biol. *68*, 75–83. https://doi.org/10.1016/j.semcancer.2019.10.007.
13. Bi, J., Khan, A., Tang, J., Armando, A.M., Wu, S., Zhang, W., Gimple, R.C., Reed, A., Jing, H., Koga, T., et al. (2021). Targeting glioblastoma signaling and metabolism with a re-purposed brain-penetrant drug. Cell Rep. *37*, 109957. https://doi.org/10.1016/j.celrep.2021.109957.
14. Chouinard, G., Lehmann, H.E., and Ban, T.A. (1970). Pimozide in the treatment of chronic schizophrenic patients. Curr. Ther. Res. Clin. Exp. *12*, 598–603.
15. Chouinard, G., and Annable, L. (1982). Pimozide in the treatment of newly admitted schizophrenic patients. Psychopharmacology (Berl) *76*, 13–19. https://doi.org/10.1007/BF00430747.
16. Sallee, F.R., Pollock, B.G., Stiller, R.L., Stull, S., Everett, G., and Perel, J.M. (1987). Pharmacokinetics of pimozide in adults and children with Tourette's syndrome. J. Clin. Pharmacol. *27*, 776–781. https://doi.org/10.1002/j.1552-4604.1987.tb02995.x.
17. Shapiro, A.K., and Shapiro, E. (1982). Clinical efficacy of haloperidol, pimozide, penfluridol, and clonidine in the treatment of tourette syndrome. Adv. Neurol. *35*, 383–386.
18. Oprescu, M., Dimitriu, V., and Simionescu, L. (1979). Serum and pituitary prolactin variations under the influence of pyridoxine and pimozide in the male rat. Endocrinologie *17*, 113–117.
19. Currò, C.T., Nicocia, G., Ziccone, V., Ciacciarelli, A., Russo, G., Toscano, A., Terranova, C., and Girlanda, P. (2022). Pimozide and pancreatic cancer in diabetic chorea: a case report. Int. J. Neurosci. *132*, 1217–1220. https://doi.org/10.1080/00207454.2021.1879063.
20. Subramaniam, D., Angulo, P., Ponnurangam, S., Dandawate, P., Ramamoorthy, P., Srinivasan, P., Iwakuma, T., Weir, S.J., Chastain, K., and Anant, S. (2020). Suppressing STAT5 signaling affects osteosarcoma growth and stemness. Cell Death Dis. *11*, 149. https://doi.org/10.1038/s41419-020-2335-1.
21. Meyer, N., Henkel, L., Linder, B., Zielke, S., Tascher, G., Trautmann, S., Geisslinger, G., Münch, C., Fulda, S., Tegeder, I., and Kögel, D. (2021). Autophagy activation, lipotoxicity and lysosomal membrane permeabilization synergize to promote pimozide- and loperamide-induced glioma cell death. Autophagy *17*, 3424–3443. https://doi.org/10.1080/15548627.2021.1874208.
22. Neifeld, J.P., Tormey, D.C., Baker, M.A., Meyskens, F.L., Jr., and Taub, R.N. (1983). Phase II trial of the dopaminergic inhibitor pimozide in previously treated melanoma patients. Cancer Treat Rep. *67*, 155–157.
23. DeBerardinis, R.J., Mancuso, A., Daikhin, E., Nissim, I., Yudkoff, M., Wehrli, S., and Thompson, C.B. (2007). Beyond aerobic glycolysis: transformed cells can engage in glutamine metabolism that exceeds the requirement for protein and nucleotide synthesis. Proc. Natl. Acad. Sci. USA *104*, 19345–19350. https://doi.org/10.1073/pnas.0709747104.
24. Hensley, C.T., Wasti, A.T., and DeBerardinis, R.J. (2013). Glutamine and cancer: cell biology, physiology, and clinical opportunities. J. Clin. Invest. *123*, 3678–3684. https://doi.org/10.1172/JCI69600.
25. Wanders, D., Hobson, K., and Ji, X. (2020). Methionine Restriction and Cancer Biology. Nutrients *12*, 684. https://doi.org/10.3390/nu12030684.
26. Yuan, H., Wu, X., Wu, Q., Chatoff, A., Megill, E., Gao, J., Huang, T., Duan, T., Yang, K., Jin, C., et al. (2023). Lysine catabolism reprograms tumour immunity through histone crotonylation. Nature *617*, 818–826. https://doi.org/10.1038/s41586-023-06061-0.
27. Meng, Q., Lu, Y.X., Wei, C., Wang, Z.X., Lin, J.F., Liao, K., Luo, X.J., Yu, K., Han, Y., Li, J.J., et al. (2022). Arginine methylation of MTHFD1 by PRMT5 enhances anoikis resistance and cancer metastasis. Oncogene *41*, 3912–3924. https://doi.org/10.1038/s41388-022-02387-7.
28. Stockwell, B.R. (2022). Ferroptosis turns 10: Emerging mechanisms, physiological functions, and therapeutic applications. Cell *185*, 2401–2421. https://doi.org/10.1016/j.cell.2022.06.003.

29. Jiang, X., Stockwell, B.R., and Conrad, M. (2021). Ferroptosis: mechanisms, biology and role in disease. Nat. Rev. Mol. Cell Biol. *22*, 266–282. https://doi.org/10.1038/s41580-020-00324-8.

30. Tang, Q., Liu, M., Liu, Y., Hwang, R.D., Zhang, T., and Wang, J. (2021). NDST3 deacetylates alpha-tubulin and suppresses V-ATPase assembly and lysosomal acidification. EMBO J. *40*, e107204. https://doi.org/10.15252/embj.2020107204.

31. Geng, F., Zhong, Y., Su, H., Lefai, E., Magaki, S., Cloughesy, T.F., Yong, W.H., Chakravarti, A., and Guo, D. (2023). SREBP-1 upregulates lipophagy to maintain cholesterol homeostasis in brain tumor cells. Cell Rep. *42*, 112790. https://doi.org/10.1016/j.celrep.2023.112790.

32. Geng, F., Cheng, X., Wu, X., Yoo, J.Y., Cheng, C., Guo, J.Y., Mo, X., Ru, P., Hurwitz, B., Kim, S.H., et al. (2016). Inhibition of SOAT1 Suppresses Glioblastoma Growth via Blocking SREBP-1-Mediated Lipogenesis. Clin. Cancer Res. *22*, 5337–5348. https://doi.org/10.1158/1078-0432.CCR-15-2973.

33. Wu, X., Geng, F., Cheng, X., Guo, Q., Zhong, Y., Cloughesy, T.F., Yong, W.H., Chakravarti, A., and Guo, D. (2020). Lipid Droplets Maintain Energy Homeostasis and Glioblastoma Growth via Autophagic Release of Stored Fatty Acids. iScience *23*, 101569. https://doi.org/10.1016/j.isci.2020.101569.

34. Guo, D., Reinitz, F., Youssef, M., Hong, C., Nathanson, D., Akhavan, D., Kuga, D., Amzajerdi, A.N., Soto, H., Zhu, S., et al. (2011). An LXR agonist promotes glioblastoma cell death through inhibition of an EGFR/AKT/SREBP-1/LDLR-dependent pathway. Cancer Discov. *1*, 442–456. https://doi.org/10.1158/2159-8290.CD-11-0102.

35. Guo, D., Bell, E.H., and Chakravarti, A. (2013). Lipid metabolism emerges as a promising target for malignant glioma therapy. CNS Oncol. *2*, 289–299. https://doi.org/10.2217/cns.13.20.

36. Guo, D., Bell, E.H., Mischel, P., and Chakravarti, A. (2014). Targeting SREBP-1-driven lipid metabolism to treat cancer. Curr. Pharmaceut. Des. *20*, 2619–2626. https://doi.org/10.2174/13816128113199990486.

37. Geng, F., and Guo, D. (2017). Lipid droplets, potential biomarker and metabolic target in glioblastoma. Intern. Med. Rev. *3*. https://doi.org/10.18103/imr.v3i5.443.

38. Cheng, X., Li, J., and Guo, D. (2018). SCAP/SREBPs are Central Players in Lipid Metabolism and Novel Metabolic Targets in Cancer Therapy. Curr. Top. Med. Chem. *18*, 484–493. https://doi.org/10.2174/1568026618666180523104541.

39. Cheng, C., Geng, F., Cheng, X., and Guo, D. (2018). Lipid metabolism reprogramming and its potential targets in cancer. Cancer Commun. *38*, 27. https://doi.org/10.1186/s40880-018-0301-4.

40. Ru, P., Hu, P., Geng, F., Mo, X., Cheng, C., Yoo, J.Y., Cheng, X., Wu, X., Guo, J.Y., Nakano, I., et al. (2016). Feedback Loop Regulation of SCAP/SREBP-1 by miR-29 Modulates EGFR Signaling-Driven Glioblastoma Growth. Cell Rep. *16*, 1527–1535. https://doi.org/10.1016/j.celrep.2016.07.017.

41. Guo, D. (2016). SCAP links glucose to lipid metabolism in cancer cells. Mol. Cell. Oncol. *3*, e1132120. https://doi.org/10.1080/23723556.2015.1132120.

42. Brown, M.S., Radhakrishnan, A., and Goldstein, J.L. (2018). Retrospective on Cholesterol Homeostasis: The Central Role of Scap. Annu. Rev. Biochem. *87*, 783–807. https://doi.org/10.1146/annurev-biochem-062917-011852.

43. Cheng, C., Ru, P., Geng, F., Liu, J., Yoo, J.Y., Wu, X., Cheng, X., Euthine, V., Hu, P., Guo, J.Y., et al. (2015). Glucose-Mediated N-glycosylation of SCAP Is Essential for SREBP-1 Activation and Tumor Growth. Cancer Cell *28*, 569–581. https://doi.org/10.1016/j.ccell.2015.09.021.

44. Castro-Mondragon, J.A., Riudavets-Puig, R., Rauluseviciute, I., Lemma, R.B., Turchi, L., Blanc-Mathieu, R., Lucas, J., Boddie, P., Khan, A., Manosalva Pérez, N., et al. (2022). JASPAR 2022: the 9th release of the open-access database of transcription factor binding profiles. Nucleic Acids Res. *50*, D165–D173. https://doi.org/10.1093/nar/gkab1113.

45. Rauluseviciute, I., Riudavets-Puig, R., Blanc-Mathieu, R., Castro-Mondragon, J.A., Ferenc, K., Kumar, V., Lemma, R.B., Lucas, J., Chèneby, J., Baranasic, D., et al. (2024). JASPAR 2024: 20th anniversary of the open-access database of transcription factor binding profiles. Nucleic Acids Res. *52*, D174–D182. https://doi.org/10.1093/nar/gkad1059.

46. Cheng, C., Geng, F., Li, Z., Zhong, Y., Wang, H., Cheng, X., Zhao, Y., Mo, X., Horbinski, C., Duan, W., et al. (2022). Ammonia stimulates SCAP/Insig dissociation and SREBP-1 activation to promote lipogenesis and tumour growth. Nat. Metab. *4*, 575–588. https://doi.org/10.1038/s42255-022-00568-y.

47. Gutiérrez-de-Juan, V., López de Davalillo, S., Fernández-Ramos, D., Barbier-Torres, L., Zubiete-Franco, I., Fernández-Tussy, P., Simon, J., Lopitz-Otsoa, F., de Las Heras, J., Iruzubieta, P., et al. (2017). A morphological method for ammonia detection in liver. PLoS One *12*, e0173914. https://doi.org/10.1371/journal.pone.0173914.

48. Chen, W.W., Freinkman, E., Wang, T., Birsoy, K., and Sabatini, D.M. (2016). Absolute Quantification of Matrix Metabolites Reveals the Dynamics of Mitochondrial Metabolism. Cell *166*, 1324–1337.e11. https://doi.org/10.1016/j.cell.2016.07.040.

49. Jacob, F., Ming, G.L., and Song, H. (2020). Generation and biobanking of patient-derived glioblastoma organoids and their application in CAR T cell testing. Nat. Protoc. *15*, 4000–4033. https://doi.org/10.1038/s41596-020-0402-9.

50. Vantaggiato, C., Panzeri, E., Citterio, A., Orso, G., and Pozzi, M. (2019). Antipsychotics Promote Metabolic Disorders Disrupting Cellular Lipid Metabolism and Trafficking. Trends Endocrinol. Metabol. *30*, 189–210. https://doi.org/10.1016/j.tem.2019.01.003.

51. McBrayer, S.K., Mayers, J.R., DiNatale, G.J., Shi, D.D., Khanal, J., Chakraborty, A.A., Sarosiek, K.A., Briggs, K.J., Robbins, A.K., Sewastianik, T., et al. (2018). Transaminase Inhibition by 2-Hydroxyglutarate Impairs Glutamate Biosynthesis and Redox Homeostasis in Glioma. Cell *175*, 101–116.e25. https://doi.org/10.1016/j.cell.2018.08.038.

52. Cheng, X., Geng, F., Pan, M., Wu, X., Zhong, Y., Wang, C., Tian, Z., Cheng, C., Zhang, R., Puduvalli, V., et al. (2020). Targeting DGAT1 Ameliorates Glioblastoma by Increasing Fat Catabolism and Oxidative Stress. Cell Metabol. *32*, 229–242.e8. https://doi.org/10.1016/j.cmet.2020.06.002.

53. Kou, Y., Geng, F., and Guo, D. (2022). Lipid Metabolism in Glioblastoma: From De Novo Synthesis to Storage. Biomedicines *10*, 1943. https://doi.org/10.3390/biomedicines10081943.

54. Geng, F., and Guo, D. (2024). SREBF1/SREBP-1 concurrently regulates lipid synthesis and lipophagy to maintain lipid homeostasis and tumor growth. Autophagy *20*, 1183–1185. https://doi.org/10.1080/15548627.2023.2275501.

55. Ianevski, A., Giri, A.K., and Aittokallio, T. (2020). SynergyFinder 2.0: visual analytics of multi-drug combination synergies. Nucleic Acids Res. *48*, W488–W493. https://doi.org/10.1093/nar/gkaa216.

56. Mao, P., Joshi, K., Li, J., Kim, S.H., Li, P., Santana-Santos, L., Luthra, S., Chandran, U.R., Benos, P.V., Smith, L., et al. (2013). Mesenchymal glioma stem cells are maintained by activated glycolytic metabolism involving aldehyde dehydrogenase 1A3. Proc. Natl. Acad. Sci. USA *110*, 8644–8649. https://doi.org/10.1073/pnas.1221478110.

57. Wang, H.M., Zhang, C.Y., Peng, K.C., Chen, Z.X., Su, J.W., Li, Y.F., Li, W.F., Gao, Q.Y., Zhang, S.L., Chen, Y.Q., et al. (2023). Using patient-derived organoids to predict locally advanced or metastatic lung cancer tumor response: A real-world study. Cell Rep. Med. *4*, 100911. https://doi.org/10.1016/j.xcrm.2022.100911.

58. Prasad, C.B., Oo, A., Liu, Y., Qiu, Z., Zhong, Y., Li, N., Singh, D., Xin, X., Cho, Y.J., Li, Z., et al. (2024). The thioredoxin system determines CHK1 inhibitor sensitivity via redox-mediated regulation of ribonucleotide reductase activity. Nat. Commun. *15*, 4667. https://doi.org/10.1038/s41467-024-48076-9.

59. He, L., Li, F., Yin, X., Bohman, P., Kim, S., McClain, C.J., Feng, W., and Zhang, X. (2019). Profiling of Polar Metabolites in Mouse Feces Using Four Analytical Platforms to Study the Effects Of Cathelicidin-Related

Antimicrobial Peptide in Alcoholic Liver Disease. J. Proteome Res. *18*, 2875–2884. https://doi.org/10.1021/acs.jproteome.9b00181.

60. Tautenhahn, R., Patti, G.J., Rinehart, D., and Siuzdak, G. (2012). XCMS Online: a web-based platform to process untargeted metabolomic data. Anal. Chem. *84*, 5035–5039. https://doi.org/10.1021/ac300698c.
61. Wei, X., Shi, X., Kim, S., Patrick, J.S., Binkley, J., Kong, M., McClain, C., and Zhang, X. (2014). Data dependent peak model based spectrum deconvolution for analysis of high resolution LC-MS data. Anal. Chem. *86*, 2156–2165. https://doi.org/10.1021/ac403803a.
62. Sud, M., Fahy, E., Cotter, D., Azam, K., Vadivelu, I., Burant, C., Edison, A., Fiehn, O., Higashi, R., Nair, K.S., et al. (2016). Metabolomics Workbench: An international repository for metabolomics data and metadata, metabolite standards, protocols, tutorials and training, and analysis tools. Nucleic Acids Res. *44*, D463–D470. https://doi.org/10.1093/nar/gkv1042.
63. Zhong, Y., Qin, Y., Yu, H., Yu, J., Wu, H., Chen, L., Zhang, P., Wang, X., Jia, Z., Guo, Y., et al. (2015). Avian influenza virus infection risk in humans with chronic diseases. Sci. Rep. *5*, 8971. https://doi.org/10.1038/srep08971.
64. Fan, Y., Zhang, R., Wang, C., Pan, M., Geng, F., Zhong, Y., Su, H., Kou, Y., Mo, X., Lefai, E., et al. (2024). STAT3 activation of SCAP-SREBP-1 signaling upregulates fatty acid synthesis to promote tumor growth. J. Biol. Chem. *300*, 107351. https://doi.org/10.1016/j.jbc.2024.107351.

STAR★METHODS

KEY RESOURCES TABLE

REAGENT or RESOURCE	SOURCE	IDENTIFIER
Antibodies		
Cleaved Caspase 3 (Asp175)	Cell Signaling Technology	Cat #: 9661; RRID: AB_2341188
Cleaved Caspase-9 (Asp330)	Cell Signaling Technology	Cat #: 9501; RRID: AB_331424
Rabbit Anti-PARP monoclonal antibody	Cell Signaling Technology	Cat #: 9532; RRID: AB_659884
Rabbit anti-COX IV (3E11) monoclonal antibody	Cell Signaling Technology	Cat #: 4850; RRID: AB_2085424
Goat anti-Rabbit IgG (H + L) Highly Cross-Adsorbed Secondary Antibody, Alexa Fluor 568	Thermo Fisher Scientific	Cat #: A-11036; RRID: AB_10563566
Goat anti-Mouse IgG (H + L) Cross-Adsorbed Secondary Antibody, Alexa Fluor 568	Thermo Fisher Scientific	Cat #: A-11004; RRID: AB_2534072
Goat anti-Rabbit IgG (H + L) Highly Cross-Adsorbed Secondary Antibody, Alexa Fluor 488	Thermo Fisher Scientific	Cat #: A-11034; RRID: AB_2576217
HA-Tag (C29F4)	Thermo Fisher Scientific	Cat #: 3724S; RRID: AB_1549585
SCD1 (M38)	Thermo Fisher Scientific	Cat #: 2438S; RRID: AB_823634
CD71 (D7G9X)	Thermo Fisher Scientific	Cat #: 13113S; RRID: AB_2715594
FASN (C20G5)	Thermo Fisher Scientific	Cat #: 3180S; RRID: AB_2100796
Horse Anti-Mouse IgG Antibody (H + L), Biotinylated	Vector Laboratories	Cat #: BA-2000; RRID: AB_2313581
Horse Anti-Rabbit IgG Antibody (H + L), Biotinylated	Vector Laboratories	Cat #: BA-1100; RRID: AB_2336201
ASCT2 (SLC1A5)	Sigma-Aldrich	Cat #: HPA035240; RRID: AB_10604092
Mouse Anti-β-Actin Monoclonal Antibody	Sigma-Aldrich	Cat #: A1978; RRID: AB_476692
Monoclonal Anti-Flag® M2 antibody	Sigma-Aldrich	Cat #: F3165; RRID: AB_259529
GLS	Abcam	Cat #: ab93434; RRID: AB_10561964
Anti-Ki67 antibody [SP6]	Abcam	Cat #: ab16667; RRID: AB_302459
Cytochrome *c* antibody	BD Biosciences	Cat #: 556433; RRID: AB_396417
Mouse Anti-SREBP-1	BD Biosciences	Cat #: 557036; RRID: AB_396559
Mouse Anti-SREBP-2	BD Biosciences	Cat #: 557037; RRID: AB_396560
Normal mouse IgG	Merck Millipore	Cat #: NI03; RRID: AB_490557
Bacterial and virus strains		
Adeno-null	Geng et al.[31]	N/A
Adeno-nSREBP-1a	Geng et al.[31]	N/A
Adeno-nSREBP-1c	Geng et al.[31]	N/A
Adeno-nSREBP-2	Geng et al.[31]	N/A
Escherichia coli strain BL21 (DE3)	Thermo Fisher Scientific	Cat #: FEREC0114
Biological samples		
Glioma tumor tissue microarray (TMA)	Department of Pathology at the OSU Medical Center	https://pathology.osu.edu
Human GBM patient samples	Department of Pathology at the OSU Medical Center	https://pathology.osu.edu
Chemicals, peptides, and recombinant proteins		
Pimozide	Sigma-Aldrich	Cat #: P1793
Fluoxetine hydrochloride	Sigma-Aldrich	Cat #: F132
Haloperidol	Sigma-Aldrich	Cat #: H1512

(*Continued on next page*)

Continued

REAGENT or RESOURCE	SOURCE	IDENTIFIER
Imipramine hydrochloride	Sigma-Aldrich	Cat #: I7379
Clozapine	Sigma-Aldrich	Cat #: C6305
Olanzapine	Sigma-Aldrich	Cat #: O1141
Perphenzaine	Sigma-Aldrich	Cat #: P6402
Promazine hydrochloride	Sigma-Aldrich	Cat #: P6656
Sulpiride	Sigma-Aldrich	Cat #: S2190000
(L-γ-Glutamy-*p*-nitroanilide) hydrochloride (GPNA)	Sigma-Aldrich	Cat #: G6133
Dimethyl sulfoxide (DMSO)	Sigma-Aldrich	Cat #: 67-68-5
6-Diazo-5-oxo-L-norleucine (DON)	Sigma-Aldrich	Cat #: D2141
Cholesterol Oxidase from microorganisms	Sigma-Aldrich	Cat #: C8868
B-27 serum-free Supplement	Thermo Fisher Scientific	Cat #: 17504044
TrypLE Express	Gibco	Cat #: 12604021
Telaglenastat (CB-839)	Adooq Bioscience	Cat #: A14396
Fatostatin	ChemBridge Corporation	Cat #: 5533803
Human epidermal growth factor (EGF)	Sigma-Aldrich	Cat #: E9644
DMEM medium without Amino Acids	MyBioSource	Cat #: MBS6120661; Lot #: L22080101
D-(+)-Glucose solution	Sigma-Aldrich	Cat #: G8644
Gibco™ L-Glutamine	Thermo Fisher Scientific	Cat #: A2916801
Gibco™ Sodium pyruvate	Thermo Fisher Scientific	Cat #: 11360070
Fibroblast growth factor (FGF)	Sigma-Aldrich	Cat #: F5392
Heparin	Sigma-Aldrich	Cat #: H3393
Non-essential Amino Acid Solution	Sigma-Aldrich	Cat #: M7145
GlutaMax	Thermo Fisher Scientific	Cat #: 35050061
HEPES	Thermo Fisher Scientific	Cat #: BP299100
Paraformaldehyde (PFA)	Sigma-Aldrich	Cat #: 158127
Hydrogen peroxide	Thermo Fisher Scientific	Cat #: H323
eBioscience™ IHC Antigen Retrieval Solution-High pH (10x)	Thermo Fisher Scientific	Cat #: 00-4956-58
Hematoxylin QS Counterstain	Vector Laboratories	Cat #: H-3404
Nessler's reagent	Ricca Chemical Company	Cat #: 5250-4
6,8-difluoro-7-hydroxy-2-oxo-2h-chromene-3-carboxylic acid	AmBreed	Cat #: 1C65038; CAS #: 215868-31-8
N-Boc-8-bromooctan-1-amine	Advanced ChemBlocks Inc	Cat #: P41296; CAS #: 142356-35-2
Dulbecco's modified Eagle's medium (DMEM)	Corning	Cat #: 15–0312 CV
DMEM/F-12 Flex Media	Thermo Fisher Scientific	Cat #: A2494301
L-Glycine	Sigma-Aldrich	Cat #: CDBC7825
L-Arginine monohydrochloride	Sigma-Aldrich	Cat #: A6969
L-Cystine dihydrochloride	Sigma-Aldrich	Cat #: C6727
L-Histidine monohydrochloride	Sigma-Aldrich	Cat #: H5659
L-Isoleucine	Sigma-Aldrich	Cat #: I7403
L-Leucine	Sigma-Aldrich	Cat #: L8000
L-Lysine monohydrochloride	Sigma-Aldrich	Cat #: L8662
L-Methionine	Sigma-Aldrich	Cat #: M5308
L-Phenylalanine	Sigma-Aldrich	Cat #: P5482
L-Serine	Sigma-Aldrich	Cat #: S4311
L-Threonine	Sigma-Aldrich	Cat #: T8441
L-Tryptophan	Sigma-Aldrich	Cat #: T8941

(*Continued on next page*)

Continued

REAGENT or RESOURCE	SOURCE	IDENTIFIER
L-Tyrosine	Sigma-Aldrich	Cat #: T8566
L-Valine	Sigma-Aldrich	Cat #: V0513
Bromophenol blue sodium salt	Sigma-Aldrich	Cat #: B8026
Methanol	Thermo Fisher Scientific	Cat #: BPA412P4
Lenti-X Concentrator	Clontech	Cat #: 631231
TRIzolTM Reagent	Invitrogen	Cat #:15596018
TWEEN® 80	Sigma-Aldrich	Cat #:P8074
Critical commercial assays		
PowerUpTM SYBRTM Green Master Mix	Applied Biosystems	Cat #: A25778
Qproteome Mitochondria Isolation Kit	QIAGEN	Cat #: 37612
LysoSensor™ Yellow/Blue dextran	Thermo Fisher Scientific	Cat #: L22460
DQ-green BSA	ThermoFisher Scientific	Cat #: D12050
BODIPY™ 493/503	Thermo Fisher Scientific	Cat #: D3922
LysoTracker™ Red DND-99	Thermo Fisher Scientific	Cat #: L7528
Low-Density Lipoprotein from Human Plasma, BODIPY™ FL-LDL complex	Thermo Fisher Scientific	Cat #: L3483
Rhodamine 123	Thermo Fisher Scientific	Cat #: R302
CellROX™ Deep Red reagent	Thermo Fisher Scientific	Cat #: C10422
MitoTracker™ Green FM Dye	Thermo Fisher Scientific	Cat #: M7514
Free fatty acid assay Kit (Quantification)	Abcam	Cat #: ab65341
Cardiolipin assay Kit	Sigma-Aldrich	Cat #: MAK362
Amplex Red Cholesterol Assay Kit	Invitrogen	Cat #: A12216
Glutaminase (GLS) Activity Assay Kit (Fluorometric)	Abcam	Cat #: ab284547
BCA protein assay kit II	Abcam	Cat #: ab287853
RIPA lysis buffer	Thermo Fisher Scientific	Cat #: NC9484499
EDTA-free Protease Inhibitor Cocktail	Sigma-Aldrich	Cat #: 11836170001
Phosphatase inhibitor	Sigma-Aldrich	Cat #: 4906837001
Hoechst 33342 Solution	Thermo Fisher Scientific	Cat #: 62249
Glo Lysis buffer	Promega	Cat #: E266A
Promega Renilla-Glo™ Luciferase Assay System	Thermo Fisher Scientific	Cat #: PRE2710
X-tremeGENETM HP DNA Transfection Reagent	Sigma-Aldrich	Cat #: 6366236001
ECL kit	Cytiva Amersham	Cat #: RPN2106
iScript cDNA Synthesis Kit	Bio-rad	Cat #: 170-8891
Deposited data		
Metabolomics data	This paper	NMDR: ST003362 Project DOI: https://doi.org/10.21228/M8QJ9B
Experimental models: Cell lines		
GBM patient-derived primary cell, GBM30	The Ohio State University	N/A
GBM patient-derived primary cell, GBM6	Mayo clinic	N/A
GBM patient-derived primary cell, GBM26	Mayo clinic	N/A
Human GBM cell: U251	Sigma-Aldrich	Cat #: 09063001;
Human GBM cell: U87	Sigma-Aldrich	Cat #: 89081402;
Human GBM cell: U373	Sigma-Aldrich	Cat #: 08061901;
Human GBM cell: T98	ATCC	Cat #: #CRL-1690™ ATCC;
Human GBM cell: LN229	ATCC	Cat #: CRL-2611™;
Human embryonal kidney cell: 293FT	Invitrogen™	Cat #: R70007
Experimental models: Organisms/strains		
Athymic NCr-nu/nu, outbred, NCI stock	Charles River Lab	Strain # 553

(*Continued on next page*)

CellPress
OPEN ACCESS

Continued

REAGENT or RESOURCE	SOURCE	IDENTIFIER
Oligonucleotides		
shSREBP-1 #1 (TRCN0000414192)	This paper	AGACATGCTTCAGCTTATCAA
shSREBP-1 #2 (TRCN0000422088)	This paper	TGAGGCTCCTGTGCTACTTTG
shSREBP-2 #1 (TRCN0000020668)	This paper	GACCTGAAGATCGAGGACTTT
shSREBP-2 #2 (TRCN0000020666)	This paper	GCAACAACAGACGGTAATGAT
shASCT2 #1 (TRCN0000043118)	This paper	CTGGATTATGAGGAATGGATA
shASCT2 #2 (TRCN0000288922)	This paper	GCCTGAGTTGATACAAGTGAA
Primers for RT-qPCR (Human)	This paper	See method details
Primers for ASCT2 promoter (Human)	This paper	See method details
Primers for Chip assay (Human)	This paper	See method details
Recombinant DNA		
pLKO.1	Addgene	RRID: Addgene_24150
pMD2.G	Addgene	RRID: Addgene_12259
psPAX2	Addgene	RRID: Addgene_12260
pGEX-GST-mCherry-D4H*	Geng et al.[31]	N/A
pRL Renilla Luciferase Control Reporter Vectors	Promega	Cat #: E2261
Software and algorithms		
GraphPad Prism Ver. 9.41	GraphPad Software	https://www.graphpad.com/features
TCGA (The Cancer Genome Atlas)	National Cancer Institute	https://www.cancer.gov/ccg/research/genome-sequencing/tcga
SynergyFinder	Ianevski et al.[55]	https://synergyfinder.fimm.fi/
Biorender	Biorender	https://www.biorender.com/
JASPAR[2024]	Rauluseviciute et al.[45]	https://jaspar.elixir.no/
ITK-SNAP (Version 3.8.0)	The Ohio State University	N/A
Chem draw	NCH Software	N/A
ZEN 2 (blue edition)	Zeiss	https://www.zeiss.com/microscopy/us/downloads.html
ImageJ	ImageJ	https://imagej.net/Downloads
Microsoft Excel	Microsoft	https://www.microsoft.com/en-us/microsoft-365/excel

EXPERIMENTAL MODEL AND STUDY PARTICIPANT DETAILS

Cell lines and culture

Authenticated (short tandem repeat profiling) human GBM cell lines, U251 (Male) and U373 (Male) from Sigma, U87 (HTB-14) (Female), T98 (CRL-1690) (Male), LN (CRL-2611) (Female) cells American Type Culture Collection (ATCC) were cultured in Dulbecco's modified Eagle's medium (DMEM), supplemented with 5% HyClone fetal bovine serum (FBS), and 4 mM glutamine.

Authenticated GBM30 (Female), GBM6 (Male) and GBM26 (Male) are primary GBM patient-derived cell lines that were previously molecularly characterized and described.[56] They were cultured in SILAC Advanced DMEM/F-12 Flex Media supplemented with 1× B-27 serum-free supplements, 2 mg/mL heparin, 2 mM glutamine, 50 ng/mL EGF, and 50 ng/mL fibroblast growth factor (FGF). GBM30-luc cells stably express luciferase (luc) and were previously described.[46] All cells were maintained at 37 °C with 5% CO_2. Cell lines in this study have different morphologies and growth rates, and any signs of contamination were constantly monitored. All cell lines used in this study were free from mycoplasma contamination based on PCR detection and were regularly maintained with mycoplasma reagent.

Clinical samples

The collection and analysis of human tissue were approved by The Ohio State University Institutional Review Board (IRB) under ref. 2015C0067. The clinical specimens were collected under a waiver of consent as the specimens are de-identified to recipient investigators. Individual glioma tumor and adjacent brain tissues, glioma tumor tissue microarray (TMA) containing 47 paired (tumors and matched adjacent brain tissues) and 176 unpaired glioma tumor tissues were from the Department of Pathology at the OSU Medical Center. Frozen normal brain tissues were obtained from cerebral autopsy samples from non-cancer individuals. Neuro-pathology

reports showed that the brain tissues were normal. All samples tested negative for HIV and hepatitis B. The details of patients' information, i.e., gender and age, are included in Table S1. TMA slides were scanned using ScanScope and analyzed using ImageScope v11 software (Aperio Technologies, Vista, CA, USA). The staining intensity of tissues was graded as 0, 1+, 2+, or 3+.

Intracranial and subcutaneous xenograft models

For GBM orthotopic xenograft model, 5×10^4 patient-derived neurosphere GBM30 cells expressing luciferase in 5 μL PBS were intracranially injected into 5–6 week old female and male athymic nude mice (NCr-nu/nu, Charles River Lab strain #553), which are immune-compromised and lack T-cells, using a stereotactic system. Tumor growth was monitored at day 7 and day 18 after injection by using an OSU Small Animal Imaging Core and Magnetic Resonance Imaging (MRI), respectively. Seven mice were injected for each group. For drug treatment, pimozide (15, 25 mg/kg/day), GPNA (60 mg/kg/day), CB-839 (20 mg/kg/day) were formulated with DMSO (final concentration 10%), and then Tween-80 (final concentration 10%, Sigma, 9005656) in PBS; Fatostatin (20 mg/kg/day) was formulated with DMSO and Tween-80 in 0.9% Sodium Chloride (McKesson Medical-Surgical, #R5201-01) and administrated to mice by intraperitoneal (i.p.) injection when tumors were established 7 days after implantation. Mice were observed until they became moribund, at which point they were sacrificed. Survival until the onset of neurologic symptoms was applied for survival curves.

For subcutaneous xenograft models, 200×10^4 GBM30 cells were subcutaneously injected into 6 week-old female athymic nude mice. Drugs were treated when tumor size reached approximately 80 mm^3. Mice weight was measured every day and tumor size was measured every two days. Tumor volume was calculated by the formula: ½×Short×Short×Long. Mice were housed 5 per cage in a conventional barrier facility on a 12 h light/dark cycle at 22°C with free access to water and food. All animals were maintained within the barrier vivarium facilities under highest level of sterility and routinely monitored for health status per OSU IACUC guidelines, and not treated with any drug or test article unless specified. All mice experiments were performed according to the protocols approved by the Institutional Animal Care and Use Committee at The Ohio State University (ref. 2011A00000064-R4).

Organoid culture

GBM patient tumors were dissociated using a human tumor dissociation kit (Miltenyi Biotech; Cat# 130-095-929) following the manufacturer's protocol. Dissociated tissue was filtered via a 70 μm filter and subjected to isolation of human tumor cells using a human cancer cell isolation kit (Miltenyi Biotech; Cat#130-108-339). These tumor cells were cultured in ultra-low plate with SILAC Advanced DMEM/F-12 Flex Media supplemented with 1×B-27 serum-free supplements, 2 mg/mL heparin, 2 mM glutamine, 50 ng/mL EGF, and 50 ng/mL fibroblast growth factor (FGF) according to a previously published protocol.[57,58] The diameter of the organoids was measured with ImageJ. To detect the degree of cell death in organoids, organoid medium was supplemented with Hoechst 33342 (10 μg/mL) (Invitrogen, Cat#H21486), Calcein AM (5μM) (Invitrogen; cat#C3100MP) and PI (10 μg/mL) (Invitrogen; Cat#P1304MP) and incubated for 1 h under the growth condition. Organoids were then imaged on an Echo Revolve fluorescence microscope. The intensity of each organoid's PI was measured with ImageJ.

The cell viability was measured by CellTiter-Glo luminescent cell viability assay according to manufacturer instructions.

METHOD DETAILS

Synergy prediction

For synergy analysis, individual values of relative cell viability from each well were measured and analyzed using online SynergyFinder web application.[55] Synergy scores < -10, from -10 to 10, and >10 indicate an antagonistic, additive, and synergistic effect, respectively.

Colony growth assay

The colony growth ability of U251, GBM30, and U373 cells was determined after pimozide treatment with or without different amino acids in full DMEM medium (containing 15 amino acids), i.e., L-Glutamine (4 mM), L-Glycine (0.4mM), L-Arginine monohydrochloride (0.4 mM), L-Cystine dihydrochloride (0.2 mM), L-Histidine monohydrochloride (0.2 mM), L-Isoleucine (0.8 mM), L-Leucine (0.8 mM), L-Lysine monohydrochloride (0.8 mM), L-Methionine (0.2 mM), L-Phenylalanine (0.4 mM), L-Serine (0.4 mM), L-Threonine (0.8 mM), L-Tryptophan (0.8 mM), L-Tyrosine (0.4 mM), L-Valine (0.8 mM).

Cells were first seeded at the density of 2000 cells/well into the 6-well plate and incubated for 6 days in full DMEM medium with 5% FBS until cell colonies were formed (medium was changed every 3 days). Cell medium was then replaced with a fresh DMEM medium without amino acids, in which 14 amino acids from the above list was added, skipping one amino acid each well, respectively, with 1% FBS added in this medium. Pimozide (3 μM) was added into medium to treat for 8 days (medium was changed every 3 days). The medium was pre-warmed in the incubator, which minimizes disturbance to cells caused by medium change. Three replicates were performed for each condition. After 8 days of treatment, colonies were fixed and stained with 1% bromophenol blue sodium salt in 80% methanol for 1 h at room temperature. Then the samples were washed completely with double distilled water and imaged by a GE Amersham Imager 600. Colony numbers were counted by ImageJ.

Stable isotope $^{13}C_5$-glutamine labeling, polar metabolite and long chain fatty acid sample preparation

300 × 10^4 U251 cells were seeded in a 15-cm dish for 24 h, then treated with/without Pimozide (3 μM) in a fresh medium containing 1%FBS, 5 mM glucose, 4 mM glutamine for another 24 h. After drug treatment, cells were deprived for 1 h with a serum-free medium containing 5 mM glucose, 0 mM glutamine, and 1 mM pyruvate. 2 mM $^{13}C_5$-glutamine was added to the media and incubated for 1h. The cells were washed twice with cold PBS and quenched with cold acetonitrile and ultrapure water (4:3, v/v) for 5 min.

Polar metabolites were extracted from the cells using a two-phase liquid-liquid extraction method. Cells were homogenized for 1 min using a Sonic Dismembrator (Fisher Scientific, USA). The homogenized sample was transferred into a 15-mL glass tube, and chloroform was added to the glass tube to make the final solvent, chloroform/acetonitrile/water (2: 4: 3, v/v/v). The mixture was then vortexed for 3 min and centrifuged at 2300 ×*g* for 8 min. The upper layer was transferred to a fresh tube and lyophilized overnight. The dried sample was reconstituted in 50% acetonitrile and vigorously vortex-mixed for 3 min. The supernatant was transferred into an autosampler vail after centrifugation at 18,000 ×*g*, 4°C for 20 min for 2DLC-MS analysis.

For long chain fatty acid extraction, cells were homogenized for 1 min. After centrifugation at 18,000 ×*g*, 4°C for 20 min, the supernatant was transferred into a micro centrifuge tube and lyophilized overnight. The dried sample was reconstituted in 200 μL 50% ethanol, and loaded onto an OASIS HLB Cartridge (Waters Corp., Milford, MA, USA). The long chain fatty acids were eluted using 600 μL of acetonitrile/methanol (90:10, v/v) after washing with 1 mL of 5% methanol. The eluate was dried under the nitrogen gas flow, reconstituted into 25 μL 75% ethanol, and transferred to an autosampler vial for LC-MS analysis.

LC-MS analysis and data processing

All samples were analyzed on a Thermo Q Exactive HF Hybrid Quadrupole-Orbitrap Mass Spectrometer coupled with Thermo DIONEX UltiMate 3000 UHPLC system (Thermo Fisher Scientific, Waltham, MA, USA). For polar metabolite profiling, the LC system was equipped with a reversed phase column (RPC, a Waters Acquity UPLC HSS T3 column, 2.1 × 150 mm, 1.8 μm) and a hydrophilic interaction chromatography column (HILIC, a Millipore SeQuant ZIC-cHILIC column, 2.1 × 150 mm, 3 μm). The two chromatographic columns were configured to form a parallel 2DLC-MS system. The mobile phases, gradient, flow rate and column temperature were same with our previous study.[59] All samples were analyzed in a random order in positive (+) and negative (−) modes to obtain full MS data for metabolite quantification. For metabolite identification, a pooled sample of each group was analyzed by 2DLC-MS/MS in positive and negative modes at three collision energies, 20, 40, and 60 eV. For analysis of long chain fatty acids, the LC system was equipped with a reversed phase column (RPC, a Waters Acquity UPLC BEH C8 column, 2.1 × 100 mm, and 1.7 μm). Water with 0.1% acetic acid was used as mobile phase A, and acetonitrile with 0.1% acetic acid was as mobile phase B. The flow rate was 0.4 mL/min. The gradient was started with 30% B, held for 3 min, increased to 99% B at 20 min, held for 5 min; then held at 30% B from 25.1 to 28 min. The column temperature was 40°C. All samples were analyzed in negative (−) modes to obtain full MS data and a pooled sample of each group was analyzed by LC-MS/MS in negative modes at three collision energies, 20, 40, and 60 eV.

For LC-MS data analysis, XCMS software was used for spectrum deconvolution[60] and MetSign software for metabolite identification, cross-sample peak list alignment, normalization, and statistical analysis.[59,61] To identify metabolites, 2DLC-MS/MS data was first matched to our in-house database that contains parent ion m/z, MS/MS spectra, and retention time of authentic standards. Threshold for spectral similarity was set $\geq$0.4, while thresholds of retention time difference and m/z variation window were respectively set $\leq$0.15 min and $\leq$5 ppm 2DLC-MS/MS data without a match with the metabolites in the in-house database were further analyzed using Compound Discoverer software (v 2.0, Thermo Fisher Scientific, Germany), where MS/MS spectra similarity score threshold was set $\geq$40 with a maximum score of 100. Those date are included in National Metabolomics Data Repository (NMDR), the Metabolomics Workbench.[62]

Synthesis of Pacific blue-labeled pimozide

Synthesis of *tert*-butyl (8-(3-(1-(4,4-bis(4-fluorophenyl)butyl)piperidin-4-yl)-2-oxo-2,3-dihydro-1H-benzo[*d*]imidazol-1-yl)octyl) carbamate (SOH-I-185-01): To the solution of 1-(1-(4,4-bis(4-fluorophenyl)butyl)piperidin-4-yl)-1,3-dihydro-2H-benzo[*d*]imidazol-2-one (1.0 eq) in DMF, was added NaH (1.2 eq) and stirred for 15 min. Then, *tert*-butyl (6-bromohexyl)carbamate (1.0 Eq) was added to the reaction mixture and stirred overnight. The reaction mixture was dissolved in EtOAc and water and extracted with EtOAc (3 × 25 mL). The collective organic layer was dried over Na_2SO_4 and concentrated on reduced vapor pressure. The residue was purified by combi flash using 0–100% EtOAc in Hexane gradient (62% yield): ^{1}H-NMR (400 MHz, $CDCl_3$) δ 8.01 (bs, 2H), 7.26–7.24 (m, 2H), 7.20–7.15 (m, 3H), 7.08–6.94 (m, 6H), 4.48–4.32 (m, 2H), 3.90–3.82 (m, 3H), 3.12–2.88 (m, 2H), 2.44–2.34 (m, 3H), 2.08–2.00 (m, 3H), 1.78–1.68 (m, 8H), 1.63–1.59 (m, 12H), 1.49–1.43 (m, 8H); (LC-MS (ESI) m/z calculated for $C_{41}H_{54}F_2N_4O_3$: 688.4164, observed [M + H]: 689.60.

Synthesis of 1-(8-aminooctyl)-3-(1-(4,4-bis(4-fluorophenyl)butyl)piperidin-4-yl)-1,3-dihydro 2H-benzo[*d*]imidazol-2-one (SOH-I-185-02): To the solution of *tert*-butyl (8-(3-(1-(4,4-bis(4-fluorophenyl)butyl)piperidin-4-yl)-2-oxo-2,3-dihydro-1H-benzo[*d*]imidazol-1-yl)octyl)carbamate (1.0 eq) in DCM, was added 4N HCl in dioxane (4 eq) and stirred for overnight. The reaction mixture was concentrated on rotavapor and diluted with DCM and neutralized with diluted ammonia and adjusted the pH to 7. The reaction mixture was extracted 10% MeOH in DCM (3 × 25 mL). The collective organic layer was dried over Na_2SO_4 and concentrated on reduced vapor pressure. The residue was utilized for the next step without purification.

Synthesis of N-(8-(3-(1-(4,4-bis(4-fluorophenyl)butyl)piperidin-4-yl)-2-oxo-2,3-dihydro-1H-benzo[*d*]imidazol-1-yl)octyl)-6,8-difluoro-7-hydroxy-2-oxo-2H-chromene-3-carboxamide (SOH-I-188-01): To the solution of 6,8-difluoro-7-hydroxy-2-oxo-2H-chromene-3-carboxylic acid in DMF, was added HBTU (1.5 eq), DIPEA (1. 1 Eq), and stirred for 15 min. Then, 1-(8-aminooctyl)-3-(1-(4,4-bis(4-fluorophenyl)butyl)piperidin-4-yl)-1,3-dihydro-2H-benzo[d] imidazol-2-one (1.0 Eq) was added to the reaction mixture and stirred overnight. The reaction mixture was purified by loaded on combi flash using a reverse phase column and 90-10% water in acetonitrile gradient (42% yield, Light yellow solid): ^{1}HNMR (400 MHz, $CDCl_3$) δ 8.77–8.71 (m, 2H), 7.38 (d, *J* = 8.0 Hz, 1H), 7.13–7.05 (m, 6H), 7.00–6.90 (m, 6H), 4.72–4.66 (m, 1H), 3.89–3.82 (m, 3H), 3.64–3.61 (m, 2H), 3.45–3.40 (m, 2H), 3.03–2.75 (m, 9H), 2.12–1.96 (m, 4H), 1.84–1.55 (m, 6H), 1.32 (bs, 6H); ^{13}CNMR (100 MHz, DMSO-d_6) δ 163.3, 162.4, 162.1, 159.8, 153.2, 143.3, 143.2, 141.2, 129.9, 129.8, 129.7, 129.5, 116.14, 121.3, 121.0, 115.7, 115.5, 109.4, 109.2, 108.9, 108.6, 52.0, 48.8, 32.3, 29.6, 29.0, 28.8, 28.0, 26.7, 26.4; HRMS (ESI): calculate for ($C_{46}H_{48}F_4N_4O_5$+ H^+), 813.36336; found, 813.26321; (M + H^+).

Synthesis of 6,8-difluoro-7-hydroxy-N-octyl-2-oxo-2H-chromene-3-carboxamide (SOH-I-203-01): To the solution of 6,8-difluoro-7-hydroxy-2-oxo-2H-chromene-3-carboxylic acid in DMF, was added HBTU (1.5 eq), DIPEA (1. 1 Eq), and stirred for 15 min. Then, octan-1-amine (1.0 Eq) was added to the reaction mixture and stirred overnight. The reaction mixture was directly loaded on combi flash and purified by using a reverse phase column and 90-10% water in acetonitrile gradient (52% yield, Colorless solid): ^{1}HNMR (400 MHz, DMSO-d_6) δ 8.70 (bs, 1H), 8.49 (d, *J* = 5.2 Hz, 1H), 7.66 (dd, *J* = 1.6 Hz, 1.6 Hz, 1H), 1.44 (t, *J* = 6.4 Hz, 2H), 1.21–1.18 (m, 12H), 0.78 (t, *J* = 6.8 Hz, 3H); ^{13}CNMR (100 MHz, DMSO-d_6) δ 161.3, 160.1, 150.6, 147.5, 141.0, 140.9, 140.5, 140.4, 138.0, 138.0, 116.7, 111.0, 111.0, 110.85, 110.82, 109.9, 109.84, 31.6, 29.4, 29.1, 29.0, 26.8, 22.5, 14.4; (LC-MS (ESI) m/z calculated for $C_{18}H_{21}F_2NO_4$: 353.143, observed [M + H]: 354.3.

Cell proliferation

3×10^4 cells/well were seeded in 12-well plates, and washed with PBS after 24 h, followed by addition of fresh medium with 1% FBS, 5 mM glucose and 1mM pyruvate and supplemented with or without 3 μM pimozide, 1 mM GPNA,100 nM CB-839, 10 μM DON or/and 4 mM glutamine for 1, 2, 3, 4 days. Live cells were counted at the indicated times using a hemocytometer after trypan blue staining.

Sphere formation assay

A total of 2000 GBM30 cells were incubated in neurobasal medium with 1×B-27 serum-free supplements, 2 mg/mL heparin, 2 mM glutamine, 50 ng/mL EGF, and 50 ng/mL FGF in a humidified atmosphere with 5% CO_2 at 37 °C. The number of spheres were counted 3 days and 6 days after cell seeding and treatment. All the experiments were performed in triplicate.

Preparation of Cell membrane fractions

Cell membranes were isolated as previously described.[43] Briefly, cells were washed once with PBS and harvested by scraping. Cells were resuspended in a buffer containing 10 mM HEPES-KOH (pH 7.6), 10 mM KCl, 1.5 mM $MgCl_2$, and 1 mM sodium EDTA, 1 mM sodium EGTA, 250 mM sucrose and a mixture of protease inhibitors, 5 μg/mL pepstatin A, 10 μg/mL leupeptin, 0.5 mM Phenylmethanesulfonyl fluoride (PMSF), 1 mM DTT (DL-Dithiothreitol), and 25 μg/mL ALLN (Calpain Inhibitor I) for 30 min on ice. Extracts were passed through a 22G × 1-1/2 inch needle 30 times and centrifuged at 900 × *g* at 4°C for 5 min to remove nuclei. The supernatants were centrifuged at 20,000 × *g* for 20 min at 4°C. For subsequent western blot analysis (for ASCT2 and CD71 protein), the pellet was dissolved in 0.1 mL of SDS lysis buffer (10 mM Tris-HCl pH 6.8, 100 mM NaCl, 1% (v/v) SDS, 1 mM sodium EDTA, and 1 mM sodium EGTA) and designated ''membrane fraction''. The membrane fraction was incubated at 37°C for 30 min, and protein concentration was determined by reading SpectraMax Plus 384 (Molecular Devices). One μL of bromophenol blue solution (100×) was added before the samples were subjected to SDS-PAGE. All chemicals were purchased from Sigma.

Mitochondria and cytosol Fractionation

The mitochondrial proteins were prepared using Qproteome Mitochondria Isolation Kit (QIAGEN, #37612) following the manufacturer's instructions. Briefly, cells were harvested and washed with PBS, and resuspended with Lysis buffer and incubated at 4°C for 10 min. The cells were centrifuged at 1,000 × *g* at 4°C for 10 min, and the supernatants were used as the cytosolic fractions. Pellets were resuspended in disruption buffer and disrupted by using a 21G needle and a syringe. Following a centrifugation at 1,000 × *g* at 4°C for 10 min, the supernatants were transferred to new tubes and centrifuged at 6,000 × *g* at 4°C for 10 min. The pellets containing mitochondria were resuspended in mitochondria storage buffer and centrifuged at 6,000 × *g* at 4°C for 20 min. Pellets were then resuspended in mitochondria storage buffer and protein concentration was determined.

Western blotting

Cells were lysed by RIPA lysis buffer containing an EDTA-free Protease Inhibitor Cocktail and phosphatase inhibitor. The proteins were separated by using 12% SDS-PAGE and transferred onto an ECL nitrocellulose membrane (GE Healthcare, #RPN3032D). After blocking for 1 h in 5% nonfat dry milk (Lab Scientific bioKEMIX, #M-0842) diluted in TBS with Tween (TBST) (Thermo Fisher Scientific, #AAJ77500K8),[63,64] the membranes were incubated with various primary antibodies, followed by secondary antibodies conjugated to horseradish peroxidase. The immunoreactivity was revealed by use of an ECL kit.

Quantitative real-time PCR

Total RNA was isolated with TRIzol according to the manufacturer's protocol, and cDNA was synthesized with the iScript cDNA Synthesis Kit. Quantitative real-time PCR was performed with iQ SYBR Green Supermix using the Applied Biosystems (ABI) 7900HT Real-Time PCR System (Appliedbiosystems QuantStudio 6 Pro). The expression was normalized to the 36B4 housekeeping gene and calculated with the comparative method ($2^{-\Delta\Delta Ct}$). The primers sequences are available as follows:

ASCT2 forward: 5′- CCGCTTCTTCAACTCCTTCAA-3′
reverse: 5′- ACCCACATCCTCCATCTCCA-3′
GLS forward: 5′-TGACTTCTCAGGGCAGTTTG-3′
reverse: 5′- GACCAGCACATCATACCCATAA-3′
36B4 forward: 5′-AATGGCAGCATCTACAACCC-3′
reverse: 5′-TCGTTTGTACCCGTTGATGA-3′

Lysosomal pH measurements

The lysosomal pH values in U251 and GBM30 cells were measured using ratiometric probes LysoSensor Yellow/Blue dextran. In brief, 6×10^4 cells were plated in a glass-bottom plate and incubated, protected from light, with 1 mg/mL LysoSensor Yellow/Blue dextran for 24 h under normal culture conditions before pimozide treatment. Confocal images were taken using a Zeiss LSM510 Meta confocal microscopy. The excitation wavelength was set to ~405 nm. Images were captured under both emission wavelengths, 450 ± 33 nm and 510 ± 20 nm. More than 30 cells were analyzed, and fluorescence was quantified by the ImageJ software.

Lysosome activity

Determination of lysosomal activity by DQ-green BSA (50 μg/mL). GBM30 and U251 cells were treated with or without pimozide (3μM) for 24 h in 1% FBS, 5mM glucose, 4 mM glutamine, 1 mM pyruvate medium, washed with PBS twice and then incubated with 10 μg/mL DQ-green BSA in fresh DMEM medium containing 1% FBS and 1% Non-essential Amino Acid Solution, 1% GlutaMax, and 1% HEPES for 6 h before observation by confocal microscopy. The cell nucleus was stained with Hoechst 33342. Intensity of fluorescence was determined by ImageJ software (Version 1.5Oi, Bethesda, MD, USA). Intensity of fluorescence was calculated as intensity/cell normalizing on the area of each single cell. Measures were obtained by analyzing at least 30 cells/sample for at least three different experiments.

Lipid droplets (LDs) staining and quantification

LDs were stained by incubating cells with 0.5 μM BODIPY 493/503 or/and co-stained with 50 nM LysoTracker Red DND-99 for 30 min and visualized by Zeiss LSM510 Meta confocal microscopy (63×/1.4 NA oil) and 1-μm-wide z-stacks acquired. At least 30 cells in each group were analyzed, and LDs numbers were quantified with the ImageJ software (NIH) in a 3D stack, as previously described.[31,32]

Low-density lipoprotein (LDL) uptake and quantification

Low-Density Lipoprotein from Human Plasma, BODIPY FL-LDL complex was used to study LDL uptake and hydrolysis, which is large protein complex (~500,000 Da) that binds to LDL receptor on the surface of vertebrate cells and delivers cholesterol via receptor-mediated endocytosis. In brief, 6×10^4 cells were plated in a glass bottom 35 mm cell culture dish and incubated with the indicated drugs. Upon treatment, BODIPY FL- LDL was added to a final concentration of 1 μg/mL for cholesterol detection for 6 h and then co-stained with 50 nM LysoTracker Red DND-99 for 30 min at 37°C. After washing twice with PBS, cells were then incubated with 1μg/mL Hoechst 33342 Solution for 30 min before confocal imaging. Confocal images were taken using a Zeiss LSM510 Meta confocal microscope. More than 30 cells were analyzed, and fluorescence was quantified by the ImageJ software.

Chromatin immunoprecipitations (ChIP)

ChIP were performed using SimpleChIP Plus Enzymatic Chromatin IP Kit (Cell Signaling) by following the instruction. Briefly, cells in 15-cm dish were fixed with formaldehyde at final concentration 1% to crosslink proteins to DNA, and then incubated with glycine. Remove media and wash cells two times with ice-cold 1 × PBS, and scape cells with ice-cold 1 × PBS containing Protease Inhibitor Cocktail following centrifuge at 2,000 × *g* for 5 min at 4°C. The pellet was used for nuclei preparation and chromatin digestion. Finally, 2 μg of purified mouse anti-SREBP-1 antibody or normal mouse IgG were used for chromatin immunoprecipitation. PCR primers used for analysis of SREBP-1 binding motifs in ASCT2 are available as follows:

ASCT2 SRE1 forward: 5′-GCAATCGCAGCAGTAGTA-3′
reverse: 5′-TGAATCCAGGAGGCAGAG-3′
SRE2 forward: 5′-CAGGCTCGTCTGGAACT-3′
reverse: 5′-CATACCGCCTTGAGTGTT-3′
SRE3 forward: 5′-GACCTCCTGACCTCAAGT-3′
reverse: 5′-CTCGAATATAAAGTGCAGGTG-3′
Negative site forward: 5′- GCAATCTTGGTTCACTGCAA-3′
reverse: 5′- TGGCTGAGACAGGAGAATCA-3′

Promoter luciferase report assay

After PCR, the fragment of gene promoter of *ASCT2 (-1347/+57bp)*, *ASCT2 (-1263/+57bp)*, *ASCT2 (-553/+57bp)* and *ASCT2 (-441/+57bp)* were cloned into pGL3-basic vector at KpnI/XhoI site. Promoter construct DNA (100 ng) and renilla plasmid (20 ng) (Promega) were transfected into U251 cells by using X-tremeGENE HP DNA Transfection Reagent (Sigma) in a 12-well plate with 5% FBS full DMEM medium for 24 h then infected with adenovirus-mediated null, N-terminal SREBP-1a, -1c or −2 for another 24 h. Cells were lysed by Glo Lysis buffer and luciferase activity was measured by using Promega *Renilla*-Glo Luciferase Assay System according to the kit instruction, and the signal was detected by Promega GloMax Plate Reader.

Primer used to clone gene promoters:
ASCT2 (−1347/+57) forward: 5′-AGTGCAGTGGTGAGATCTCG-3′
reverse: 5′-GTCCGGGAGTAGCGGTTACC-3′
ASCT2 (−1263/+57) forward: 5′-GGATTACAGGCATGTGCCAC-3′
reverse: 5′-GTCCGGGAGTAGCGGTTACC-3′
ASCT2 (−553/+57) forward: 5′-CGCTTCACCTCCCAAAGTGG -3′
reverse: 5′-GTCCGGGAGTAGCGGTTACC-3′
ASCT2 (−441/+57) forward: 5′-CCTGCACTTTATATTCGAGG-3′
reverse: 5′-GTCCGGGAGTAGCGGTTACC-3′

Production and infection of Lentivirus-shRNA

Mission pLKO.1-puro lentivirus vector containing shRNA for shSREBP1 (#1: TRCN0000414192; #2: TRCN0000422088), shSREBP-2 (#1: TRCN0000020668; #2: TRCN0000020666), shASCT2 (#1: TRCN0000043118; #2: TRCN00000288922) and the non-mammalian shRNA control (Addgene, SHC002) were purchased from Sigma. The shRNA vector and packing plasmids psPAX2 and the envelope plasmid pMD2.G were transfected into 293FT cells using the polyethyleneimine (Polysciences, 23966). Supernatants were harvested at 48 h and 72 h and concentrated using the Lenti-X Concentrator (Clontech, 631232). The virus titer was quantified by real-time PCR by using qPCR Lentivirus Titration Kit. The lentiviral transduction was performed according to Sigma's MISSION protocol with polybrene (8 μg/mL). GBM cells were infected with the same multiplicity of infection (MOI) of shControl, shSREBP-1, shSREBP-2 or shASCT2 lentivirus.

Immunofluorescence (IF)

Cells grown on coverslips were washed with PBS twice and fixed with 4% paraformaldehyde (PFA) for 30 min, then permeabilized with 0.1% Triton X-100/PBS for 10 min and blocked by 3% bovine serum albumin (BAS) for 30 min at room temperature. The cells were stained with primary antibodies overnight at 4°C, followed by incubation at room temperature for 2 h with the appropriate secondary antibody, including Alexa Fluor 488-labeled goat anti-Rabbit IgG (H + L), and Alexa Fluor 568-labeled goat anti-rabbit IgG (H + L). Cells were washed three times with PBS in a dark chamber. The coverslips were washed as described above, inverted, mounted on slides using ProLong Gold Antifade Mountant with DAPI (Thermo Fisher Scientific, #P36931) and examined with a Zeiss LSM510 Meta confocal microscopy.

Mitochondrial membrane potential (MMP)

MMP in cells were analyzed by use of Rhodamine 123 according to the instructions of the manufacturer. Rhodamine 123 is a cell-permeant, cationic, green-fluorescent dye that is readily sequestered by active mitochondria without cytotoxic effects. In brief, 6×10^4 cells were plated in a glass bottom 35 mm cell culture dish and incubated with the indicated drugs. After treatment, Rhodamine 123 was added to a final concentration of 0.05 μg/mL for MMP detection for 30 min at 37°C. After washing twice with PBS, cells were then incubated with 1μg/mL Hoechst 33342 Solution for 30 min before confocal imaging. Confocal images were taken using a Carl Zeiss LSM510 Meta (63x/1.4 NA oil). More than 30 cells were analyzed, and fluorescence was quantified by the ImageJ software.

Transmission electronic microscopy

Cells were fixed for 30 min in 2.5% glutaraldehyde in 0.1 M phosphate buffer, pH 7.4 containing 0.1 M sucrose, and post-fixed in 1% osmium tetroxide/phosphate buffer for 30 min at room temperature. The cells were stained en-bloc with 1% uranyl acetate for 30 min, followed by dehydration in graded ethanol series 50%, 30%, 85%, 95%, 100%, 100%. The cells were finally embedded in Eponate 12 resin. Sections (70 nm) were produced on a Leica EM UC6 ultramicrotome and stained with 2% uranyl acetate and Reynold's lead citrate. Transmission electronic microscopy (TEM) was performed on a FEI Tecnai G2 Spirit BioTWIN TEM at 80 kV.

Images were captured using an AMT camera. These experiments were performed at the OSU Microscopy Core Facility.

Seahorse analysis

The Seahorse XFe 24 Extracellular Flux Bioanalyzer (Agilent) was used to measure oxygen consumption rate (OCR) according to the manufacturer's protocol. After drugs treatment for 24 h, cells were placed into fresh DMEM medium containing 5 mM glucose, 4 mM glutamine, and 1 mM pyruvate and incubated for 1 h. Three metabolic inhibitors were sequentially loaded into each well, i.e., oligomycin (Oligo, 1 μM), followed by carbonyl cyanide 4-trifluoromethoxy-phenylhydrazone (FCCP) (2 μM), followed by rotenone (Rot, 2 μM).

Detection of reactive oxygen species (ROS)

ROS in cells were analyzed by use of the fluorogenic CellROX Deep Red reagent according to the instructions of the manufacturer. The cell-permeant CellROX Deep Red reagent is non-fluorescent in its reduced state, produces bright near-infrared fluorescence upon oxidation by ROS, and has been used to detect oxidative stress in cells. In brief, 6×10^4 cells were plated in a glass bottom 35 mm cell culture dish and incubated with the indicated drugs. Upon treatment, CellROX Deep Red reagent was added to a final concentration of 0.5 μM for ROS detection or co-stained with 50 nM MitoTracker Green FM Dye for 30 min at 37°C. After washing twice with PBS, cells were then incubated with 1 μg/mL Hoechst 33342 Solution for 30 min before confocal imaging. Confocal images were taken using a Zeiss LSM510 Meta confocal microscope. More than 30 cells were analyzed, and fluorescence was quantified by the ImageJ software.

Free fatty acid measurement

30×10^4 U251 cells were seeded in 6-cm dish for 24 h, then treated with/without drug (Pimozide: 3 μM; GPNA: 1 mM; DON: 10 μM; CB-839: 100 nM) in fresh medium with 1% FBS, 5 mM glucose, 4 mM glutamine for another 24 h. After drug treatment, cells were washed twice with cold PBS, then homogenized in 200 μL chloroform/Triton X-100 (1% Triton X-100 in pure chloroform) and incubated on ice for 30 min. After that, removed chloroform at 50°C in the fume hood. The cellular free fatty acid measurements were performed following the instruction manual of the free fatty acid assay Kit (Quantification) (#ab65341).

Cardiolipin measurement

300×10^4 U251 cells were seeded in 15-cm dish for 24 h, then treated with/without drug (Pimozide: 3 μM; GPNA: 1 mM; DON: 10 μM; CB-839: 100 nM) in fresh medium with 1%FBS, 5 mM glucose, 4 mM glutamine for another 24 h. After drug treatment, cells were washed twice with cold PBS and centrifuged at 10,000 × *g* for 10 min, then suspended cells in 100 μL CL assay buffer and sonicated on ice for 1 min. After that, centrifuged it again and transferred the supernatant to a fresh tube. The cardiolipin measurements were performed following the instruction manual of the cardiolipin assay Kit (#MAK362).

Cholesterol measurement

30×10^4 U251 cells were seeded in 6-cm dish for 24 h, then treated with/without drug (Pimozide: 3 μM; GPNA: 1 mM; DON: 10 μM; CB-839: 100 nM) in fresh medium with 1%FBS, 5 mM glucose, 4 mM glutamine for another 24 h. After drug treatment, cells were washed with PBS twice and collected by scraping and centrifugation at 1,000 rpm for 10 min. The cell pellets were resuspended in amount of Isopropanol/Triton X-100 (1% Triton X-100 in pure isopropanol) for 1 h at room temperature. After centrifugation at 12,000 rpm for 10 min, the supernatants were transferred into 12 × 75 mm ASTM Type 1, Borosilicate Glass Disposable Culture Tubes (Kimble Chase, 73500-1275) (glass tubes) and dried under nitrogen. Cholesterol measurements were performed following the instruction manual of the Amplex Red Cholesterol Assay Kit (Invitrogen, #A12216).

Glutaminase (GLS) activity measurement

30×10^4 U251 cells were seeded in 6-cm dish for 24 h, then treated with Pimozide (0, 2, 3.5 μM) in fresh medium with 1%FBS, 5 mM glucose, 4 mM glutamine for another 24 h. After drug treatment, cells were washed with PBS twice and collected by scraping and centrifugation at 1,000 rpm for 10 min. The cell pellets were resuspended in 100 μL GLS assay buffer for 10 min on the ice. After centrifugation at 10,000 × *g* for 10 min, collect the supernatants and estimate protein concentration using BCA protein assay kit II (Abcam, Cat# ab287853). Then remove small molecules using 10 kDa cut-off spin filters (Cat. No. ab93349). Glutaminase (GLS) Activity measurement was performed following the instruction manual of the Glutaminase (GLS) Activity Assay Kit (Fluorometric) (Abcam, Cat # ab284547).

Magnetic resonance imaging (MRI)

Animals were anesthetized with 2.5% isoflurane mixed with 1 L/min carbogen (95% O_2 with 5% CO_2) then maintained with 1% isoflurane. Physiological parameters, including respiration and temperature, were monitored using a small animal monitoring system (Model 1025, Small Animals Instruments, Inc. Stony Brook, NY). A pneumatic pillow was used to monitor respiration. Core temperature was maintained using circulating warm water within the animal holder. Animals were injected intraperitoneally with 0.1 M gadolinium-based contrast agent used at a ratio of 100 μL per 25 g body weight. Imaging was performed using a Bruker BioSpec 94/30USR MRI system (Bruker BioSpin, Karlsruhe, Germany) and a mouse brain circularly polarized (CP) surface coil and an 86 mm diameter CP volume coil as receiver and transceiver coils, respectively. Data were collected using a T1-weighted RARE sequence with the following acquisition parameters: TR = 1200 ms, TE = 7.5 ms, rare factor = 4, NA = 3, FOV = 20 mm × 20 mm, matrix size = 256 × 256, slice thickness = 1 mm, number of slices = 18. A T2-weighted RARE sequence was also used following T1-weighted acquisition (parameters: TR = 2500 ms, TE = 33 ms, rare factor = 8, NA = 4, FOV = 20 mm × 20 mm, matrix size = 256 × 256, slice thickness = 1 mm, number of slices = 18). For data analysis, a region of interest (ROI) that included tumors (hyper-intense regions) was outlined. Tumor volumes were calculated from the outlined ROIs. All imaging experiments were conducted at the OSU Small Animal Imaging Core.

Hematoxylin and eosin (H&E) staining

Paraffin tissue sections were deparaffinized in xylene and rehydrated in degrading ethanol dilutions (100%, 95% and 70% ethanol). After washing with distilled water (dH_2O), slides were stained with hematoxylin and eosin (H&E) solution in sequence, followed by washing with dH_2O. Then, slides were dehydrated in degraded ethanol and immersed in xylene, followed by mounting in Permount.

Immunohistochemistry (IHC)

IHC was performed as previously described.[32] Briefly, tissue sections were cut from paraffin blocks of biopsies. Tissue slides were placed in oven at 60°C for 30 min then deparaffinized in xylene 3 times for 5 min each followed by dipping in graded alcohols (100% twice, 95%, 80% and 70%) for 2 min each. Slides were washed with dH_2O 3 times for 5 min each and immersed in 3% hydrogen peroxide (Thermo Fisher Scientific, #H323) for 10 min followed by washing with dH_2O. Slides were transferred into pre-heated eBioscience IHC Antigen Retrieval Solution-High pH (10×) (Thermo Fisher Scientific, #00-4956-58) in a steamer for 30 min. After cooling, slides were washed with dH_2O and then PBS. Slides were blocked with 2% normal horse serum blocking solution (Vector Laboratories, #S-2000) at room temperature for 1 h and then incubated with primary antibody overnight at 4°C, followed by incubating with secondary antibody including Biotinylated horse Anti-Rabbit IgG Antibody (H + L) (and Biotinylated horse Anti-Mouse IgG Antibody (H + L) at room temperature for 30 min. After incubation with avidin-biotin complex, slides were washed 3 times for 5 min with PBS and stained with Vector NovaRED Substrate Kit, Peroxidase (HRP) (Vector Laboratories, #SK-4800). Next, slides were washed with tap water, counterstained with Hematoxylin QS Counterstain (Vector, #H-3404), and dipped briefly in graded alcohols (70%, 80%, 95% and 100%) then in xylene 2 times for 5 min each. Finally, slides were mounted with VectaMount permanent mounting medium (Vector, #H-5000) and imaged.

Ammonia staining

In vitro cultured cells and paraffin-embedded tissue were used for ammonia staining with Nessler's reagent (Ricca Chemical Company, #5250-4) according to the following protocol. Nessler's reagent is an aqueous yellow pale solution of potassium iodide, mercuric chloride, and potassium hydroxide used for ammonia determination. This solution becomes a darker yellow in the presence of ammonia. At higher concentrations of ammonia, a brown precipitate may form according to the following reaction[47]:

$$NH4^{+} + 2[HgI_4]^{2-} - + 4OH^{-} \rightarrow HgO \cdot Hg(NH_2)I\downarrow + 7I^{-} + 3H_2O$$

$$(\text{pale yellow})\ (\text{orange} - \text{brown})$$

For ammonia staining, *in vitro* cultured cells with or without treatment were first fixed by 4%PFA for 30 min at RT then washed with dH_2O twice, each time 5mins before staining. For paraffin embedded section (5 μm) were dewaxed in xylene 3 times (Thermo Fisher Scientific, #BPX3P1GAL) and dipped graded alcohols (100% twice, 95%, 80% and 70%). Then, sections were incubated exactly 5 min with Nessler's reagent and washed for 10 s with dH2O stirring the samples gently to develop the color. After that, samples were counterstained with Hematoxylin QS Counterstain (Vector, #H-3404) for 20 s, washed with running tap water and dehydrated in graded alcohol, and mounted with VectaMount permanent mounting medium (Vector, #H-5000).

QUANTIFICATION AND STATISTICAL ANALYSIS

For cell proliferation, and quantification of LDs and TGs, mitochondrial length and loss of cristae, quantification of ROS and TMA, and OCR, data were analyzed by unpaired Student's t test or one-way ANOVA. Kaplan-Meier plot was used for patient and mice overall survival and the difference in survivals was tested by log rank test. The mice were assigned to groups randomly. Tumor volume and weight were analyzed by one-way ANOVA. Multiplicity for each experiment was adjusted by the Holm's procedure to control for type I error rate at 0.05. The quantification of tumor volume in mice brain measured by MRI was blinded. Data analysis was performed using SAS 9.4 (SAS; Cary, NC) or GrapPad Prism 9.41 statistical software. Sample size used was based on the results from our previous studies.[32,46,52] All samples were included in the analysis.